universität wien

MASTERARBEIT / MASTER'S THESIS

Titel der Masterarbeit / Title of the Master's Thesis

„Fabrication and imaging of oxidation-free phosphorene“

verfasst von / submitted by

David Lamprecht, BSc

angestrebter akademischer Grad / in partial fulfilment of the requirements for the degree of

Master of Science (MSc)

Wien, 2023 / Vienna, 2023

Studienkennzahl lt. Studienblatt / degree programme code as it appears on the student record sheet:	A 066 876
Studienrichtung lt. Studienblatt / degree programme as it appears on the student record sheet:	Masterstudium Physik
Betreut von / Supervisor:	Univ.-Prof Dr. Jani Kotakoski

Abstract

Black phosphorous (BP) is a two-dimensional material that has attracted a huge amount of interest due to its anisotropic structure and promising electronic, optical and mechanical properties. However, BP degrades rapidly under ambient conditions, which severely limits its usefulness in applications. In order to find degradation-mitigating strategies, it is important to understand the degradation mechanisms down to the atomic scale. In this study, BP samples were produced in an inert atmosphere, and introduced into the CANVAS ultra high vacuum system without being exposed to ambient conditions. As the samples were nonetheless severely contaminated by hydrocarbon compounds, several cleaning methods were tested. Additionally, the amorphization of few-layer BP under laser irradiation was observed. The degradation mechanisms are discussed and the role of chemical etching due to reactive oxygen species in the BP surface contamination is emphasised. To increase the stability of BP under the electron beam, BP-graphene heterostructures were also produced and analyzed. The heterostructures disintegrated significantly slower than pure BP, which makes it easier to study the properties of thin BP samples.

Zusammenfassung

Schwarzer Phosphor (Phosphoren) ist ein Material aus der Klasse der niedrigdimensionalen Materialien, welches aufgrund der anisotropen Struktur und guter elektronischen, optischen und mechanischen Materialeigenschaften als zukunftsträchtiger Werkstoff für elektronische und optoelektronische Anwendungen gilt. In der Praxis ist die Anwendbarkeit von Phosphoren jedoch durch bedingte Umweltstabilität stark eingeschränkt. Um Schutzmechanismen gegen Umwelteinflüsse zu entwickeln, müssen die Mechanismen dieser Instabilität bis auf atomarer Größenordnung untersucht werden. In dieser Arbeit wurden Phosphoren Proben unter einer Argon Atmosphäre hergestellt und in einem Rasterelektronenmikroskop abgebildet. Durch die einzigartigen Eigenschaften des CANVAS ultra-hoch-Vakuum Systems können die Proben dabei ohne Kontakt zur Außenwelt transportiert, gelagert und bearbeitet werden. Eine Untersuchung der Proben ergab großflächige Kontamination durch Kohlenwasserstoffe, daher wurden einige Reinigungsmethoden getestet. Zusätzlich konnte die Amorphisierung einer dünnen Phosphoren Probe durch Laser-Bearbeitung beobachtet werden. Da Phosphoren unter Einfluss des Elektronen-Strahls Schicht-für-Schicht abgetragen wird, wurden Phosphorene-Graphen Heterostrukturen hergestellt, welche eine erhöhte Stabilität aufweisen. In einer Diskussion der Abtragungsmechanismen stellte sich chemisches Ätzen als ein wichtiger Faktor heraus. Ein signifikanter Teil der Ätzstoffe stammt dabei wahrscheinlich aus der Kontamination, welche große Teile der Proben bedeckt.

Aknowledgments

First and foremost I want to thank my supervisor Jani Kotakoski for his patience and support throughout my time in the pnm research group. He gave me freedom to implement my own ideas, provided me with the resources and tools I needed and was always there to share his knowledge.

Next I want to thank Carsten Speckmann and Clemens Mangler, who guided, supported and challenged me in basically every step of this thesis. They helped me to solve numerous technical issues and to stay motivated in spite of many setbacks. The discussion and implementation of new ideas with them was very much fun and instructive and motivated me to find new spheres of interest and to acquire new skills. Especially I want to thank Carsten for taking the time to read and correct my thesis, his feedback was extremely helpful.

Many thanks also go to Manuel Längle, Wael Joudi, Clara Kofler and Barbara Mair who entertained me while studying, taught me experimental methods, provided me with insightful information, lent a hand during experiments and brought the fun into the pnm. Furthermore I would also like to thank all my other former and present colleagues who were always helpful and created a fantastic work environment.

I am very thankful for all the support and I'm looking forward to working with many of my colleagues also on the next part of my journey.

List of acronyms

2D	two-dimensional
AC	arm-chair
ADF	annular dark field
AFM	atomic force microscopy
BP	(few layer) black phosphorous
BP/G	black phosphorous on graphene
CANVAS	controlled alteration of nanomaterials in vacuum down to the atomic scale
CBED	convergent beam electron diffraction
CCD	charge coupled device
EELS	electron energy loss spectroscopy
eV	electron volt
FFT	fast fourier transformation
FLG	few layer graphene
hBN	hexagonal boron nitride
HOPG	highly ordered pyrolytic graphite
IPA	isopropyl alcohol
PDMS	polydimethylpolysiloxane
PMMA	polymethylmethacrylat
PPC	polypropylene carbonate
STM	scanning tunneling microscope
STEM	scanning transmission electron microscope
TEM	transmission electron microscope
vdW	van der Waals
UHV	ultra high vacuum
XPS	x-ray photoelectron spectroscopy
ZZ	zig-zag

Contents

Chapter 1

Introduction

Although two dimensional (2D) materials have been studied theoretically since the late 1940s [1], it was believed that they can not exist in an unsupported state due to thermodynamical instability [2, 3]. In 2004, Novoselov and Geim were the first to successfully isolate a single layer of graphene from highly oriented pyrolitic graphite (HOPG) [4]. Due to the high electron mobility, mechanical strength and other fascinating properties found in graphene [5], 2D materials have become an extensively growing field of research. Among the first 2D materials isolated and characterized, other than graphene, were hexagonal boron nitride (hBN) and molybdenum disulfide (MoS_2) in 2005 [6]. Since then the family of 2D materials has been steadily growing. In 2013, Koenig et al. were the first to isolate 2D crystals of black phosphorus, called phosphorene, the only known free standing mono-elemental 2D material besides graphene [7]. Phosphorene has a reasonably sized and tunable direct band gap and a good carrier mobility, which allows direct integration in electronic devices, unlike graphene which has to be modified to become a semi-conductor [8].

Unfortunately phosphorene is subject to rapid degradation under ambient conditions, which is commonly attributed to chemical interaction between the phosphorene surface and ambient molecules like water vapor or gaseous oxygen. To prevent degradation of sensitive 2D structures like phosphorene they are often passivated by encapsulation in other 2D materials like hexagonal boron-nitride (hBN) [9]. To find the optimal passivating material, the degradation mechanics of phosphorene have to be investigated in great detail down to the atomic scale.

1.1 State of the art

The degradation mechanics of phosphorene (from now on BP) have been studied in various experiments over the last decade. A typical degradation study consists of various steps: Fabrication of the material, transfer to the substrate/grid, transfer to the measurement device, exposure to damaging gases and the spectroscopic or microscopic measurement itself. The exact laboratory conditions during each step are of crucial importance as even very small doses of reaction agents could alter the outcome significantly. In the following the most relevant studies on BP degradation are briefly described.

When Koenig et al. [7] isolated BP for the first time in 2013 they already observed the air induced degradation over a time frame of hours. To mitigate the degradation they covered the BP with a polymethylmethacrylat (PMMA) film while handling it under ambient conditions. This is not an ideal solution as the chemical removal of the polymer may damage the material and leave polymer residues behind.

In 2015 Huang et al. did the first systematical (scanning) transmission electron microscopy (STEM) study on ambient degradation [10]. They imaged BP samples with STEM directly after exfoliation, after one week of immersion in de-ionized (DI) water, after two days of immersion in deoxygenated water and after one day under ambient air conditions. STEM-EELS analysis of the samples could detect no oxygen signal in the freshly exfoliated samples but significant damage and a high amount of oxygen in all samples exposed to the other various conditions. This observation has to be taken with a grain of salt because a similar study by Wu et al. [11] shows clearly some amount of oxygen even minutes after exfoliation. Also the experimental conditions of Huang et al. were less than ideal due to the usage of solvents, and the fabrication and transport under ambient conditions.

A more detailed study by Favron et al. was also published in 2015 [12]. In comparison to earlier studies they produced the samples inside a nitrogen-filled glovebox before transferring them to the measurement devices. The atomic force microscopy (AFM) measurements were done under ambient conditions while Raman spectra were obtained inside a vacuum chamber with $3 \cdot 10^{-5}$ mbar base pressure. TEM samples were produced under ambient conditions. This was the first instance of measurements under controlled gas conditions as small amounts of oxygen and water vapor were introduced into the Raman vacuum chamber to study changes in the Raman spectra during the degradation process.

In 2017 Kuntz et al. [13] were the first to study BP under strict laboratory conditions. Few layer BP was fabricated inside a nitrogen-filled glovebox by liquid exfoliation in anhydrous N-Methylpyrrolidone. Then the samples were transferred inside the glovebox to TEM grids using isopropyl alcohol (IPA). To study the influence of individual gases the samples were exposed to water vapor, oxygen and ambient air before being transported to an XPS instrument. All these steps happened inside the inert atmosphere. Additionally low-resolution TEM images were obtained, whereas the exact conditions during these imaging sessions are not stated in the paper.

In 2020 Naclerio et al. [14] were the first to visualize the oxidation mechanics of BP trough in-situ TEM experiments. They introduced small amounts of water vapor and oxygen into the TEM column while continuously imaging the BP samples. They observed that the BP is stable under a 80 kV beam at the base pressure of $2.4 \cdot 10^{-7}$ mbar and only began to disintegrate once an oxygen partial pressure of $2.4 \cdot 10^{-6}$ mbar was introduced. This observation is in contradiction to similar studies (e.g. [15]) which can be explained by the thickness of the sample (13 layers) studied by Naclerio et al. and the experimental conditions. For example Naclerio et al. exfoliated the flakes directly onto TEM grids and used no inert atmosphere during fabrication and transport.

The so far most strict study has been reported by St. Laurent et al. [16] in 2021. Bulk black phosphorus was cleaved inside the UHV chamber of an scanning tunneling microscope (STM) (how exactly this was done is not specified in the publication). The STM was held at a temperature of 10 K but the vacuum level is not mentioned. Subsequently $1 \cdot 10^{-5}$ mbar of pure oxygen were introduced into the vacuum chamber and the structural changes were observed by STM. This is the first experiment showing the degradation of BP on the atomic scale.

Lee et al.[1] have published a series of papers [15, 17, 18] which are of much interest for this thesis. In the first publication [15] (2007) they were the first group to show atomic scale TEM images of BP and its edge structures. Although they fabricated the samples under inert atmosphere, their transfer method was not ideal as they used solvents and cleaned the BP flake inside a H_2/O_2 plasma.

The second and third publication [17, 18] from 2020 and 2022 are characterized by a different approach: To increase the stability of BP under the electron beam, the 2D material was covered in graphene sheets, either from one or from both sides. Also they refined their transfer technique,

[1]Note the first author of the first two papers is Yangjin Lee, whereas the first author of the 2022 paper is Sol Lee. Sol Lee is also the second author of the 2020 publication and Yangjin Lee is the second author of the 2022 paper so all three publications are attributed to "Lee et al." for the sake of convenience.

applying the PDMS transfer method, which is free from solvents or other potentially damaging preparation steps. Exfoliation and transfer happened inside a nitrogen-filled glovebox, the samples were exposed to ambient air only during the transport to the TEM. The vacuum level during 80 kV TEM imaging was $\sim 1 \cdot 10^{-7}$ mbar. Apart from imaging BP at an atomic scale they studied the stability of the material under the electron-beam, discussed the reasons for e-beam induced damage and observed self-passivating edges in bi-layered BP. Additionally the authors found in-situ annealing to be a reliable method to clean BP samples from hydro-carbon contamination. Apart from Lee et al., also Yao et al. [19] and Baboukani et al. [20] reported atomic scale imaging of BP. As both groups produced their samples under an ambient environment, they are not described here in more detail.

1.2 Motivation

As can be seen in the last section there are only few reports of atomic scale imaging of BP. Out of these reports only Lee et al. fabricated their samples with minimal oxygen exposure [17, 18]. Kuntz et al. studied the degradation of BP under in-situ exposure of ambient gases, but far from the atomic scale [13]. The goal of this study is to close the gap by imaging oxidation-free BP under a controlled atmosphere and at atomic resolution. The (so far) only facility where this could be achieved is the Vienna Sternwarte laboratory with its CANVAS system [21]. This system allows to prepare samples inside an argon-filled glovebox, to introduce samples into the UHV system without exposure to ambient conditions and to image the samples at atomic resolution and under controlled atmosphere using a custom Nion UltraSTEM 100 scanning transmission electron microscope.

In this work, few-layer BP samples are fabricated using the PDMS method. Atomic scale STEM images of BP flakes are obtained and the e-beam induced degradation is discussed. To overcome the problem of thick contamination on BP several cleaning methods are tested and a UHV annealing device is designed. Furthermore the experiments of Lee et al. are replicated.

The outcome of this thesis is the groundwork for future studies where the degradation mechanisms of clean and oxidation-free BP samples will be studied inside the controlled atmosphere of the STEM column.

Chapter 2

Materials

The main material used in this thesis is black phosphorus. Graphene is briefly described because it is used as a supporting layer in phosphorene/graphene van der Waals heterostructures.

2.1 Phosphorene

Although being the most stable allotrope of elemental phosphorus materials, black phosphorus was only discovered in 1914 by Percy Bridgman while observing white phosphorus under high pressure [22]. In white phosphorus the four atoms of a P_4 molecule form a tetrahedral structure where every atom forms three bonds with its neighbours. Due to this configuration the bonds cannot achieve the ideal 90° angle for 3p orbitals but rather form arc-like bonds which reduces the stability of white phosphorus. In BP on the other hand, the atoms form continuous layers with two in-plane sp^3 bonds with angles of 96.34° and 103.09°, respectively. These are closer to the ideal angle of 109.5° for tetragonal lattices. An additional out-of-plane bond with a 45° angle leads to the characteristic puckered honeycomb structure with two "sublayers" within every layer [8]. The lattice parameters are 4.374 Å, 3.313 Å, and 10.473 Å for a, b and c, respectively [23]. In analogy to graphene there exists a so called arm-chair (AC) direction [010] and a zig-zag (ZZ) direction [100] as can be seen in figure 2.1. The individual BP layers are bound by rather strong van der Waals-interactions (in comparison to similar 2D materials like graphene). Nevertheless cleavage of individual layers is possible [8].

Due to this unique structure BP exhibits a strong in-plane anisotropy causing many differences in the electric, mechanic and magnetic properties along the ZZ and AC direction, respectively.

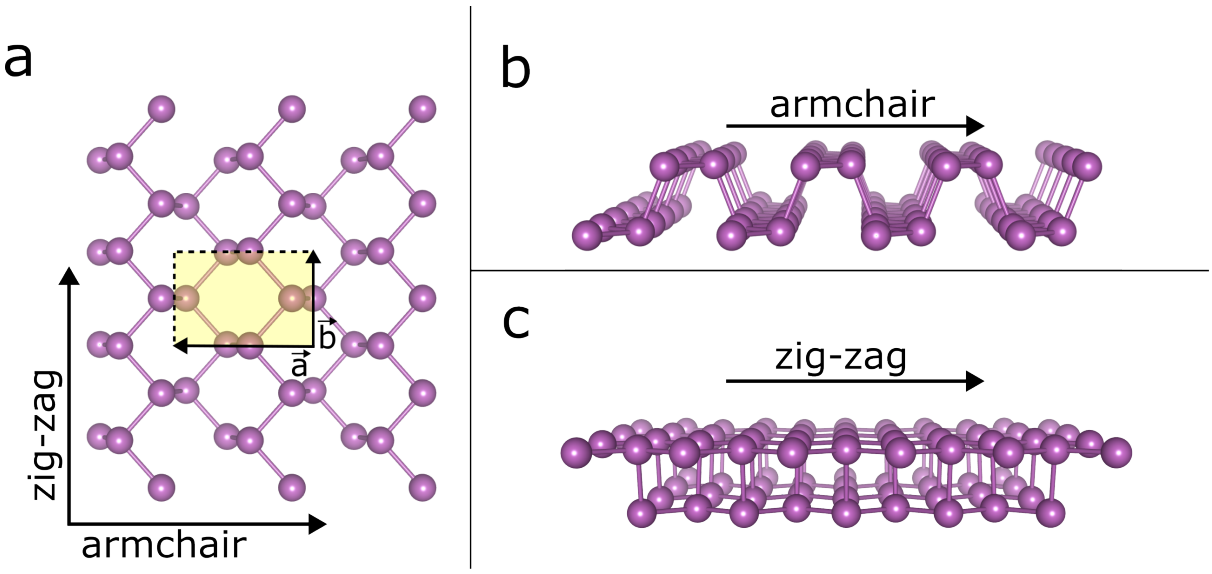

Figure 2.1: The structure of BP. a) Top down view with the unit cell and the in-plane lattice vectors $\vec{a}$ and $\vec{b}$. b) The puckered structure of BP seen in armchair direction and c) in zig-zag direction. Visualizations created using Vesta©

Most notably BP shows an eight-fold increased hole effective mass along the ZZ direction in comparison to the AC direction [24], an anisotropic electron mobility ratio of 1.5 [25] and a negative Poisson ratio in the out-of-plane direction when BP is stretched or compressed in the ZZ direction [26].

Bulk BP is a semiconductor with a small direct bandgap of ca. 0.3 eV. With decreasing layer number the bandgap blue-shifts to a monolayer bandgap of ca. 2 eV while remaining direct. Due to dominating excitonic effects the optical bandgap is much smaller than the electronic bandgap (especially in the monolayer). Nevertheless photoluminescence measurements can be used to determine the number of layers in few-layer samples [24, 27].

Due to its high anisotropy BP displays dichroism. This means light rays with different polarization are absorbed at different rates. Dichroism is especially pronounced for photons with energies close to the corresponding bandgap energy as only photons with a polarization component along the AC direction are absorbed. This happens because the symmetry of the electron wave function in the conduction and valence bands forbids absorption of light polarized along the ZZ direction. This property can be used to determine the crystallographic orientation of the sample and may be useful for selective photodetectors [8].

BP is also a promising material for a range of electrical, photoelectrical and catalytic applications.

Phosporene-based field effect transistors (FET) show better performance than MoS_2 FETs in terms of on/off ratio and charge carrier mobility [8]. Due to its thickness-depended bandgap, ranging from infrared to visible frequencies, and a high absorption in the UV region, BP is very well suited to be used in photodetectors. Such devices show a high responsivity and a short response time [28]. Additionally BP could be used as a photocatalyst to split water into H_2 and O_2 using solar energy or to convert CO_2 into less harmful molecules like CH_4 or CH_3OH [29]. Furthermore BP has a very high Seeback coefficient which makes it an interesting material for thermoelectric devices, but this advantage is mitigated by high thermal conductivity, which leads to low ZT[1] values [30].

2.1.1 Environmental stability

The main limiting factor of BP is its rapid degradation under ambient conditions. Extensive damage has been observed in a timeframe of one hour [13] and even minutes [31]. Understanding the mechanisms behind this instability has therefore become an intense area of research [8, 29]. The degradation is commonly associated with two main effects: Oxidation by environmental gases (particularly O_2 and H_2O) and morphological effects (e.g., oxidized regions affecting the oxidation mechanics in neighbouring unoxidized regions) [32]. The oxidation process of pure O_2 on pristine BP begins with the dissociation of physisorbed O_2 near the surface leading to the formation of a P_2O_3 oxide layer which is further oxidized until stable P_2O_5 is formed. The oxidation penetrates into the bulk but the degradation rate decreases with increasing oxide layer thickness as the surface oxide acts as a passivation layer. Thus, BP flakes with more than 10 layers thickness are considered air-stable, whereas oxidation in thin phosphorene flakes leads to a collapse of the crystal structure [32, 33]. The limited stability of few-layered BP has been suggested to be related to its bandstructure: The size of the mono- or bilayer phosphorene bandgap enables the formation of excitons under ambient light. These photo-generated electrons transfer from the conduction band to the O_2 molecules on the surface and generate O^-_2 radicals which are apt to react with the topmost phosphorene layer. The adsorption energy of O^-_2 molecules is four times larger than for O_2, so an abundance of radicals leads to a higher concentration of absorbed oxygen. In thicker flakes the conduction band minimum decreases until it drops below the O_2/O^-_2 redox potential, limiting the production of O^-_2 [34]. Once the molecule comes closer

[1]The ZT value, as well as the Seeback coefficent, are measures for the effectiveness of the energy conversion process in thermoelectric devices. The ZT value is indirectly proportional to the thermal conductivity and directly proportional to the electrical conductivity.

to the surface, its O-O bonds soften and the elemental oxygen binds to a phosphorus atom. This is accompanied by a conversion of the molecular unpaired triplet ground-state into a singlet state [12]. The last step of BP degradation is its dissolution via water vapor. The H atom in ambient H_2O forms a hydrogen bond with an oxygen atom on the BP surface. After a short time the O atom and its bound phosphorus atom are lifted off by the dragging water molecule, breaking the intralayer-bonds of BP. As only the uppermost layer of the BP crystal is affected by this process, BP dissolves layer-by-layer [34]. Contrary to those ambient-air-induced oxidation effects, etching with O_2 plasma [35, 33] or exposure to oxygen under an 80 kV electron-beam [13] leads to faster and more severe degradation of BP.

Both H_2O and illumination, as well as the electron beam in electron microscopy, are suspected to amplify the degradation process. While a perfectly flat sheet of pristine BP seems to be unaffected by pure H_2O exposure, water-induced degradation has been found at defects such as edges or steps leading to pitting [13]. The role of light in the oxidation process is unclear: Many theoretical studies emphasize the necessity of an additional energy source like photons (or the e-beam of an electron microscope) as a condition for oxidation [34, 36, 37], although in experiments oxidation can be found (though with a reduced rate) even when BP was stored in dark (e.g. [13]). This observation could be related to oxidation at defect sites like single- or multi-P vacancies, where much less energy is needed to induce a reaction. Oxidation at defect sites generally facilitates the formation of an amorphous oxide layer with no self-passivating capabilities and thus enhances the degradation of the BP flake [14, 37]. Furthermore degradation is faster in ZZ direction than AC direction as shown by theoretical predictions [36] and experimental studies [14, 38].

2.2 Graphene

Graphene is a 2D material made of carbon atoms with the electronic ground state configuration $1s^2 2s^2 1p_x^1 1p_y^1$. In graphene the 2s and 1p orbitals hybridize into sp^2 orbitals. The sp^2 orbitals form covalent σ bonds in plane, while one p_z orbital remains unaffected from the hybridization and forms a delocalized π band. Graphene has a planar structure where every atom binds to its three nearest neighbours in an angle of 120° forming a honeycomb lattice (figure 2.2a). The hexagonal lattice constant a is 0.246 Å and the average distance between two neighbouring atoms 0.142 Å. The strong in-plane σ bonds are responsible for the extraordinary mechanical properties

of graphene such as a high Young's modulus[2] of 1 TPa [39] (for comparison A36 mid-carbon steel has a Young's modulus of $\sim$ 200 GPa [40]).

The first Brillouin zone of graphene is depicted in figure 2.2b, it has four high symmetry points Γ, K, K' and M of which the two Dirac points K and K' play an important role in the electronic structure of the material. Using the tight-binding model, one can calculate the energy dispersion relation around those two points [41] as

$$E_{\pm}(\delta\vec{k}) = \pm\frac{\sqrt{3}\gamma_0 a}{2}|\delta\vec{k}| \; . \tag{2.1}$$

Here γ_0 is the transfer integral between two p_z orbitals and $\delta\vec{k}$ is a small shift in reciprocal space around K or K'. From this equation it becomes clear that the dispersion is linear around the Dirac points. The bottom of the conduction band and the top of the valence band touch at these points on the Fermi level (figure 2.2c) and the density of states at this spot is zero. This leads to the quasi-metallic behaviour of graphene with charge carriers moving like massless relativistic particles [42]. The electron mobility can reach values of up to $2.5 \cdot 10^5$ cm^2 V^{-1} s^{-1}, the highest for any known material at room temperature [43]. Graphene shows extraordinarily high thermal conductivity [44] and maximum current density [45]. The electronic properties of graphene depend strongly on the layer number and stacking order; bi-layered graphene exhibits a small band gap whereas thicker graphene samples show increasingly metallic behaviour [41].

A single layer of freestanding graphene absorbs about 2.3 percent of white light, making it hard to identify atomically thin layers in optical microscopy. The relative optical contrast of graphene on a substrate however is depending on the substrate and light wavelength. In the case of SiO_2 substrates it depends mainly on the substrate thickness. The contrast of a graphene layer on a 300 nm SiO_2 substrate as a function of visible light wavelength has a maximum in the green region around 550 nm and a maximal value of about 12 percent. Thus it is possible to see a single layer of graphene on SiO_2 using ambient light [46].

[2]The Young's modulus or modulus of elasticity quantifies the relation between the applied compression or extension force per unit area and the resulting axial strain (deformation) in the linear elastic region of a material.

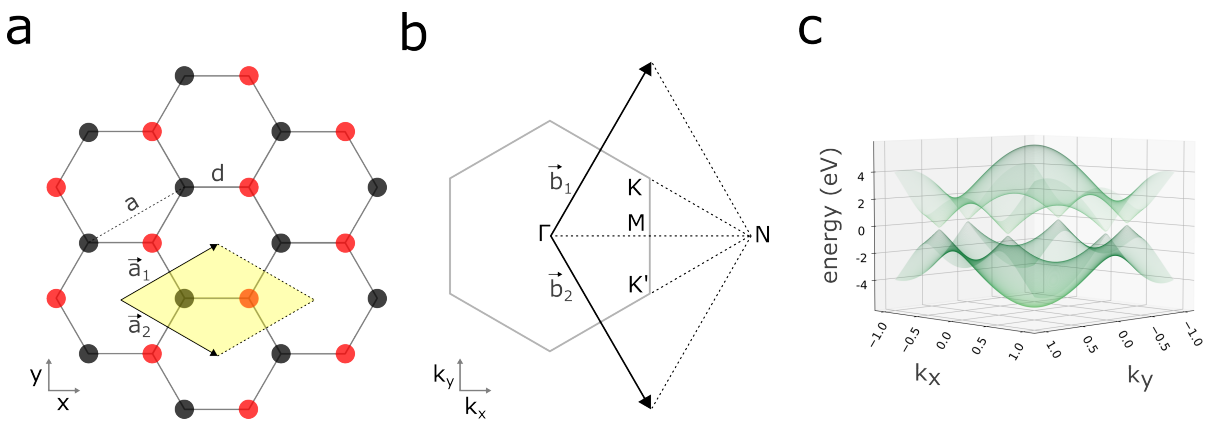

Figure 2.2: a) Crystal lattice of graphene. $\vec{a_1}$ and $\vec{a_2}$ are the unit vectors, a is the lattice constant, d the distance between neighbouring carbon atoms. The unit cell is marked in yellow. b) The first Brillouin zone with the high symmetry points Γ, K, K' and M and the reciprocal lattice vectors $\vec{b_1}$ and $\vec{b_2}$. c) The electronic dispersion relation of graphene with the Dirac cones at the K and K' points. Calculated and plotted in python using the tight-binding approximation.

2.3 van der Waals heterostructures

van der Waals (vdW) heterostructures are artificial heterojunctions created by stacking different 2D materials. The strong in-plane covalent bonds provide stability to the individual layers, whereas the weaker van der Waals forces between the layers are sufficient to keep the stacks together [47]. The increasing library of 2D materials offers a variety of possible stacking orders and allows to combine advantageous features of the single materials. For example, one may reduce the undesired effects of uneven substrates on the field effect mobility of graphene by putting it on the ultra-flat surface of hBN [48]. Encapsulation of highly reactive materials by chemically inert layers protects the sensitive materials from absorbed chemicals and ambient gases and may improve their performance. For example Doganov et al. produced FETs by covering BP with hBN layers which not only increased the environmental stability of BP but also enhanced the sub-threshold swing[3] of the FETs compared to BP on SiO_2 FETs [49]. The combination of different 2D materials in vdW heterostructures can also introduce new phenomena, like the formation of trions[4] at room temperature in WS_2–$MoSe_2$ heterostructures [50], or enable new

[3]The sub-threshold swing $S = dV_g/ln(dI_{sd})$ of a FET is a measure for how fast a transistor can be turned on or off. More specifically it is the change in gate-voltage dV_g needed to increase the current between source and drain I_{sd} one order of magnitude.

[4]Trions are quasiparticles consisting of an exciton (a bound state of an electron and a hole) and an additional charge carrier. In the case of the mentioned vdW heterostructure, the exciton is excited in the WS_2 layer and interacts with an electron from the $MoSe_2$ layer.

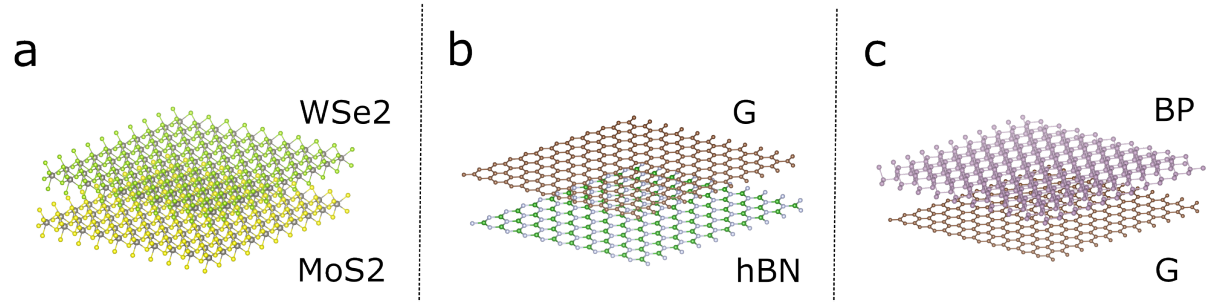

Figure 2.3: Examples of vdW heterostructures. a) A MoS_2/WSe_2 heterojunction, which is potentially useful for vertical tunneling diodes [52]. b) hBN acting as an ultra-flat substrate for graphene [48]. c) Graphene covering BP to increase its environmental stability [17]. Visualizations created using Vesta©.

devices like vertical tunnelling FETs [51]. Figure 2.3 shows a overview over the most important 2D materials as well as hBN/graphene as an example of a vdW heterostructure.

vdW heterostructures can be assembled in two principal ways: Either by exfoliating each layer individually and stacking them on each other using some kind of micromechanical transfer technique or by growing the layers directly on other 2D materials. The main advantage of the stacking approach is its flexibility as nearly every known 2D material can be used to create stacks of nearly arbitrary complexity. However these techniques have limitations in terms of scalability. Also some of those stacking techniques use sacrificial layers which have to be removed by solvents. This is an additional limitation as the usage of solvents and the residues left behind on the 2D surfaces hampers further transfer processes and might affect their properties [53]. Alternatively one may use pick-and-lift techniques like the PPC transfer technique described in this thesis. These techniques offer cleaner interfaces but are usually hard to implement and limited to a selected range of materials [54].

The second approach is growing 2D materials directly on other 2D materials using techniques like chemical vapor deposition (CVD)[5]. These techniques may use individual steps for every material, like the CVD growth of hBN using ammonia borane (NH_3-BH_3) on graphene, which itself is grown via CVD on a copper substrate using a liquid precursor [55], or may be single-step like the direct growth of WS_2/MoS_2 heterostructures on a SiO_2 substrate reported by Gong et al [56]. Whereas both approaches are usually not limited by lattice-matching constraints, CVD growth is often severely hindered by the sensitivity of 2D materials in regards to growth conditions: The optimal

[5]CVD is the chemical growth of materials on a substrate under controlled gas conditions and elevated temperatures using solid and/or liquid precursors and a stable precursor gas flow.

growth conditions for one material may be damaging for another material in the stack [53].

The physical properties of vdW stacks may not only depend on the specific stacking order but sometimes also on the lattice mismatch and relative rotation of the layers. For example the lattice constants of graphene and hBN have a mismatch of ca. 1.8 percent (both materials have the same hexagonal planar structure). If they are stacked upon each other a rotation-depended moiré pattern appears, which acts like a periodic potential and introduces new Dirac points into the electronic structure [57]. If the crystallographic directions of two similar materials are aligned, areas, where one layer is forced to match the lattice of the other layer, as well as relaxed areas with mismatching lattices can be observed [58].

Another important consideration when building vdW stacks is interlayer contamination. Unless they are produced under ultra-clean surface science conditions, every surface is covered in adsorbed species like oxygen, hydrocarbons or growth-related residues. When 2D materials are stacked together the contamination is trapped between the surfaces and one would expect it being evenly distributed not unlike glue at the interface between two pieces of wood [47]. In reality, however, the interfaces of vdW stacks are found to be atomically clean and atomically sharp as could be shown by cross-sectional TEM imaging [59] and by the appearance of moiré patterns [60]. This phenomenon can be explained by the contamination being squeezed out of the stack or forced into µm sized "dirt pockets" by the van der Waals forces which attract the adjacent crystals [47, 59].

In an atomic-force microscopy (AFM) and infrared spectroscopy (IR) study Palinkás et al. looked at the composition and structure of contamination typically found on 2D materials and found a self-organized monolayer of 20-26 carbon atom long alkane molecules on graphene, hBN and MoS_2 which forms after days of storage under ambient conditions. These molecules could also be found in the dirt pockets of vdW heterostructures, where they are stacked up to form "hills" of up to tens of nm height. Freshly exfoliated samples were also covered by contamination, but this contamination lacked structure and its molecular composition could not be identified [61]. When Schwartz et al. tried to identify the contaminants between the interfaces of dry-transfer-assembled vdW heterostructures using the photo-thermal induced resonance[6] (PTIR) technique they found absorption spectra associated with the stamp material used for the dry transfer (PDMS or PPC). Heterostructures prepared using stamps cleaned by solvents like toluene or IPA did

[6]PTIR is a technique that uses the photothermal effect induced in IR active samples by irradiating it with an IR laser, which is then measured using a visible laser. The spectra obtained by PTIR are very similar to Fourier transform infrared spectroscopy (FTIR) spectra which makes it easy to identify chemical species with a sub-µm spatial resolution.

not show any evidence of the stamp material. However, the stamp may only play a partial role as a contamination source as the cleaning procedure did not change the structure and size of the dirt pockets [62]. Khestanova et al. showed that the size and form of the "dirt pockets" between monolayers of 2D materials and atomically flat substrates are determined purely by the elastic properties of the 2D material and showed a nearly universal aspect ratio of $h_{max}/L_{eff} \propto 0.1$ between the maximal height h_{max} and the characteristic in-plane length L_{eff} of the dirt pockets [63].

Chapter 3

Methods

3.1 Scanning transmission electron microscopy

The main experimental method used in the thesis is scanning transmission electron microscopy (STEM). This section gives a brief overview over STEM and associated techniques. For more details we refer to [64] and [65].

3.1.1 Electrons as a probe

The resolution d of a microscope is ultimately limited by the Abbe diffraction limit as

$$d \geq \frac{\lambda}{n \sin(\alpha)} \tag{3.1}$$

where λ is the wavelength of the light, n the refractive index and α the collection angle . Given that the denominator of this formula is of the order of 1 for most optical microscopes, the wavelength of the light needs to be of the same order of magnitude as the interatomic spacings (1 Å) to achieve atomic resolution. This is not possible in light microscopy, but particle waves can reach such short wavelengths as the de Broglie wavelength of an accelerated particle with mass m is defined as [66]

$$\lambda = \frac{h}{mv} \, , \tag{3.2}$$

where h is the Planck constant and v the velocity of the particle. Using the relation between the momentum of the particle with charge q, accelerated by a potential U and its kinetic energy E_0, we get a non-relativistic wavelength

$$\lambda = \frac{h}{\sqrt{2mE_0qU}} \,. \tag{3.3}$$

In the relativistic case this becomes

$$\lambda = \frac{h}{\sqrt{2mE_0eU}} \frac{1}{\sqrt{1 + \frac{eU}{mc^2}}} \tag{3.4}$$

with the speed of light in vacuum being c. If we set the electronic rest mass of an electron m_0, the elemental charge e and a typical acceleration voltage of 60 kV we get a spatial resolution of $\lambda \approx 5$ pm and $\lambda \approx 4.8$ pm for the classical and relativistic case, respectively.

Equation 3.4 states that the resolution increases approximately with the square root of the particle mass, thus heavier particles like neutrons or protons can resolve smaller structures compared to electrons. Nevertheless, electrons are the most reasonable choice for most experiments because they additionally interact electromagnetically with the electronic system of the sample structures, unlike neutrons, which only interact with the nuclei via the weak nuclear force. Also neutrons and protons, as well as more exotic particles like muons and positrons, need expensive and elaborate sources like particle accelerators and suffer from the lack of suitable optics. Charged ions have become a possible choice in some cases [67] but their high momentum tends to damage the materials which is especially unfavourable in the case of low-dimensional solids, where a high concentration of defects affect the crystal structure and other properties of the sample [67].

3.1.2 Electron scattering

Usually one distinguishes two types of electron scattering: Elastic scattering, where the total kinetic energy of the system remains unchanged by the scattering event and inelastic scattering, where the particle excites internal degrees of freedom in the material, while at the same time loosing a part of its own kinetic energy. Elastic scattering is primarily used for imaging, where the change in image intensity due to deflection of the primary beam corresponds to spacial positions while inelastic scattering is used to gain information about the properties of the studied material. Examples for inelastic electron scattering techniques are electron energy-loss spectroscopy (EELS) or energy dispersive x-ray spectroscopy (EDX).

Every type of interaction has a unique cross section σ, usually given in barn [10^{-28}] m^2, which

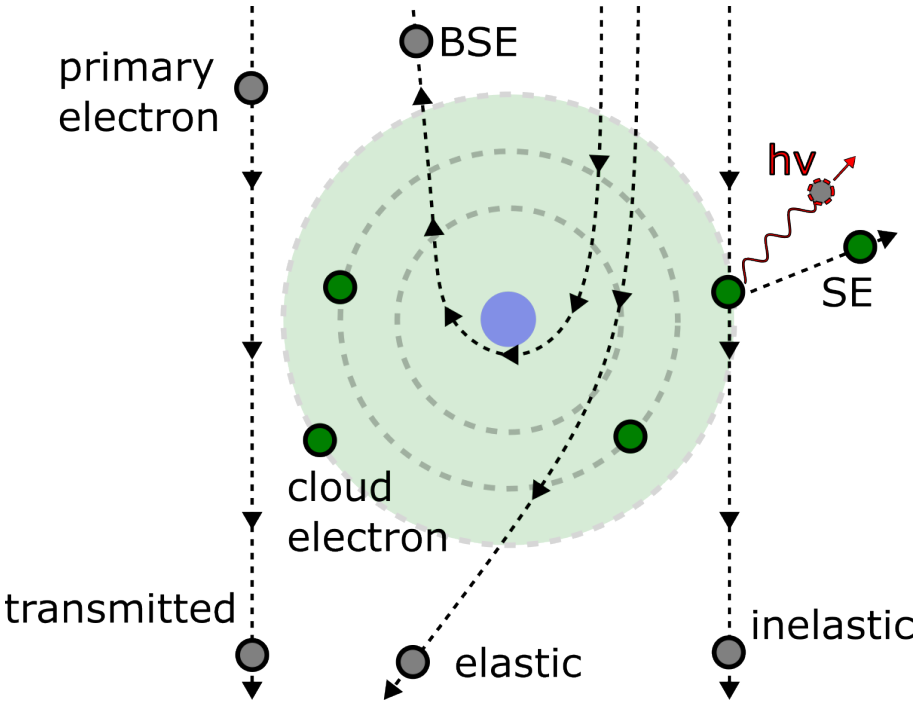

Figure 3.1: Illustration of possible interactions of primary beam electrons (grey) with the nucleus (blue) and the electron cloud (green). Primary electrons far from the nucleus are transmitted. Electrons that travel closer to the nucleus have their trajectory changed (elastical scattering). This can even result in back scattered electrons (BSE). Primary electrons can interact with the electron cloud. This may result in the emission of a photon (hv) or eject a so-called secondary electron (SE) from the atom. The interaction with the electron cloud results in a significant amount of energy loss of the primary electron (inelastic scattering). Adapted from an illustration by IndianFace and published under the GNU Free Documentation License Version 1.2

is a measure for the interaction probability. The cross section is given in units of square-meters because one may think of it as the area an electron has to hit to cause the respective interaction. Often one uses the differential cross section $d\sigma$ which provides the angular distribution of the scattering probabilities which can be integrated to obtain the cross section.

3.1.3 Inelastic scattering

There is a variety of inelastic scattering processes all related to primary electron energy-loss through the excitation of an internal degree of freedom. The electron may interact with particles like nuclei and electrons or with quasi-particles like phonons or plasmons. In the following the most important inelastic scattering processes are described.

Electron-electron scattering

Primary electrons may transfer energy when colliding with an electron in the electron cloud of an atom. Usually this interaction has a low cross section and the transferred energy is specific because the electrons are bound to the nuclei in quantized states and the impinging electron can only transfer specific amounts of energy to lift a material electron to an unoccupied state in the conduction band. This excitation leads to a state in the valence band being unoccupied. This so called "hole" can act as a positive charge carrier or recombine with an electron which is followed by the emission of a photon with characteristic wavelength. If the primary electron is able to transfer enough energy to overcome the ionization energy, it removes the bound electron from the atom, which can be collected as a so called "secondary electron", leaving behind a charged ion. If the hole left behind by the removed electron is filled by an electron from a higher shell, the relaxation energy can either be emitted as a characteristic x-ray photon or can be transferred to an another electron, which is ejected as a so called Auger electron. Secondary, Auger and backscattered electrons can be collected with specialized electron detectors and used for spectroscopy. Characteristic x-rays can be used as an analytic method in EDX. The x-ray signal is superimposed with the continuous spectrum of the bremsstrahlung which is created by the inelastic scattering of the electrons with the nuclei. The exact energy transferred between primary electrons, electrons and nuclei in the material is not only determined by the respective element and material but also by the bonding states.

Electron-quasiparticle scattering

Phonons and plasmons are collective excitations of the atoms or electrons in a solid, respectively. Phonon excitations have high cross sections and characteristic energies in the order of meV to a few eV [68]. Due to this low excitation energy the phonon energy-loss signal in EELS is usually hidden below the strong zero-loss peak and can not be resolved using the equipment available in our setup. Plasmons have energies in the range of tens of eV, broad energy spreads and reasonably high cross sections [68]. They are clearly visible in the spectrum but can not be used to characterize the materials composition.

3.1.4 Elastic scattering

If we look at the interaction between an impinging electron and a target nucleus, the scattering angle depends primarily on the distance between the electron and the nucleus, the impact param-

eter b. The smaller b the stronger the Coulomb attraction leading to higher scattering angles. For larger b the electron primarily interacts with the surrounding electron cloud. This leads to the so called screening effect, where the (negatively charged) electron cloud partially compensates the effect of the positive nucleus leading to lower scattering angles.

If we take this screening effect into account, we can calculate the differential Rutherford cross-section which is widely used for (S)TEM calculations [64]:

$$\frac{d\sigma(\theta)}{d\Omega} = \frac{Z^2\lambda^4}{64\pi^4 a_0^2} \frac{1}{\left[sin^2\left(\frac{\theta}{2}\right) + \frac{\theta_0^2}{2}\right]^2}\ , \tag{3.5}$$

where Z is the atomic number, a_0 the Bohr radius, θ the scattering angle, θ_0 the so-called screening parameter and λ the de Broglie wavelength of the incoming electron with relativistic correction from equation 3.4. The Rutherford cross section has to be modified for heavy elements ($Z > 30$) and high electron energies (above 300 keV), but this is not relevant for this study.

Equation 3.5 shows that scattering to higher angles is more likely for atoms with higher atomic numbers but less likely with higher beam electron energy. This Z-dependency can be used for Z-contrast imaging, enabling correlation between the measured intensity and the atomic number [69]. Electrons scattered to a specific range of angles are collected with ring-like detectors to detect only the scattered part of the electron beam. This is the physical principle behind annular dark field imaging (ADF), which is the standard method used in this thesis.

3.1.5 Beam damage

The interaction between energetic electrons and the sample can lead to structural damage in the material. The specific magnitude of the created damage depends strongly on the primary beam energy and is material-specific. Usually one distinguishes two principal damaging mechanisms, radiolysis, associated with inelastic scattering and knock-on damage, related to elastic scattering.

An impinging electron can interact with the electron cloud and excite electrons to higher shells or remove them entirely. This perturbation of the electromagnetic equilibrium can weaken or break up bonds and create defects in the crystal structure. This process, radiolysis, is typical for materials with a bandgap like semi-conductors or insulators where neighbouring electrons are trapped in the atomic potential well [68]. Metals do not suffer from this damaging mechanism because local empty states can easily be filled by mobile electrons. The calculation of the radiolysis

cross-section is non-trivial as one has to consider many variables of a multi-particle system.

The second damage mechanism, knock-on damage, stems from the elastic collision of the impinging electron with the nuclei. If an electron is able to transfer enough energy to the nucleus, the atom will be displaced from the structure, consequently creating point defects. The energy needed to allow such displacements is called the displacement threshold and is specific for a certain atom and material. The maximum amount of energy T_{max} a primary electron with kinetic energy E_0 can transfer to a stationary atom with mass M occurs at a backscattering event and is given by

$$T_{max} = \frac{2E_0(E_0 + 2m_0c^2)}{Mc^2} \,. \tag{3.6}$$

However atoms are not stationary but move with velocity v in the out of plane direction. Therefore this formula needs to be adapted to [70]

$$T_{max} = \frac{\left(2\sqrt{E_0(E_0 + 2m_0c^2)} + Mvc\right)^2}{Mc^2} \,. \tag{3.7}$$

These equations are based on the approximation that the electron mass is much smaller than the target mass and that the kinetic energy of the impinging electron is negligible in comparison to the rest energy mc^2 of the atom. If the maximum transferable energy is higher than the displacement threshold of an atom, the impinging electron may remove the atom from the material. Applying equation 3.6 for this thesis, one can see that a 60 keV electron can transfer ca. 4.5 eV of energy to a phosphorus atom. The knock-on threshold for a phosphorus atom in a pristine lattice is approximately 6 eV in the ground state [71]. Consequently, an acceleration voltage of 60 kV seems to be a reasonable choice to avoid extensive knock-on damage. Note that the knock-on thresholds at defect sites or edges are typically lower than in a pristine lattice, thus some amount of knock-on damage is unavoidable. Knock-on damage can also occur below the knock-on threshold if the material is in an excited state. This can be expected to be an important damaging pathway in BP as experiments with other 2D semiconductors like MoS_2 show significant knock-on damage also below the displacement threshold [72, 73].

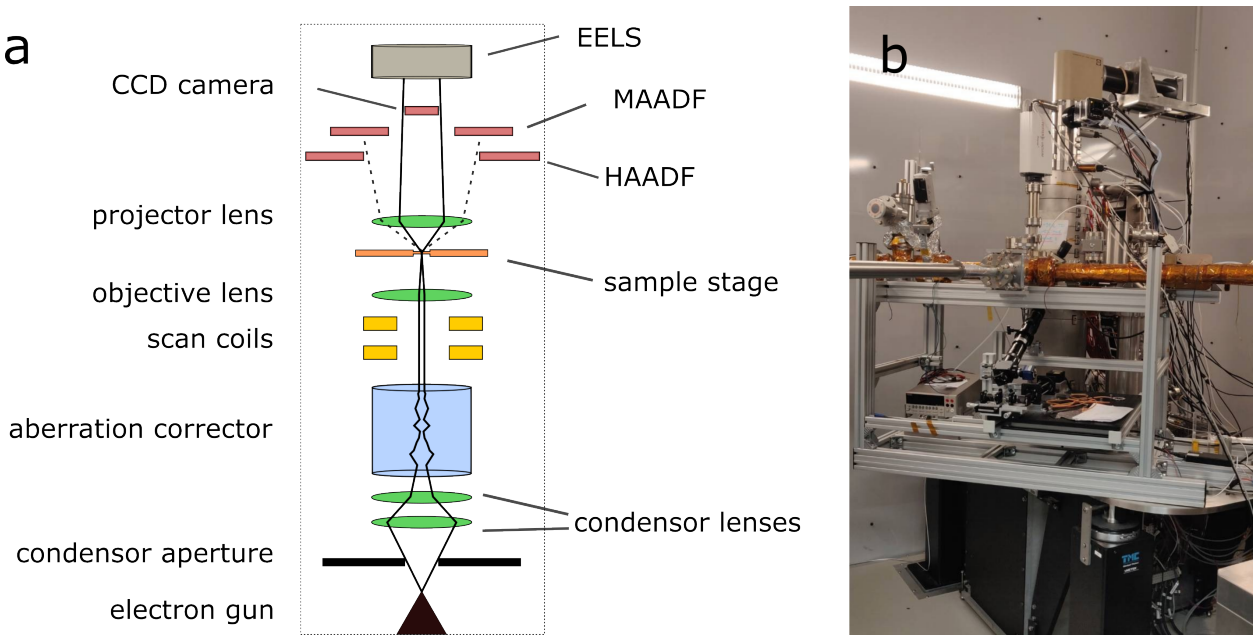

Figure 3.2: a) Schematic illustration of a scanning transmission electron microscope. The beam goes from bottom to top. b) The Nion UltraSTEM 100 at the laboratory at Sternwarte, Vienna. The pipes in the front connect the STEM to the rest of the UHV system.

3.1.6 Scanning transmission electron microscopy (STEM)

In STEM, a focused electron beam is scanned across the sample, the transmitted electrons are collected for every probe position and the intensity at every position is arranged into an image. The basic building blocks of a STEM are the electron source, a system of lenses to focus the beam and correct for aberrations, the scanning coils, the sample stage and electron detectors as well as spectroscopic tools. Figure 3.2a shows a schematic drawing of the Nion UltraSTEM 100 used in this thesis. In the following, the individual parts of the microscope are described in more detail.

Electron Source

The Nion UltraSTEM 100 is equipped with a cold field emission gun as the electron source. It consists of a sharpened tungsten tip which is held at a high negative potential relative to a nearby anode. This potential gradient allows electrons to overcome the material's potential well (work function) and to quantum tunnel into free space where they are accelerated to the operational energy (e.g. 60 keV) via a second anode. As the anodes act like electromagnetic lenses, the beam has its first crossover point right after the electron source, as can be seen in figure 3.2a. In comparison to older thermionic emitters, field emission guns are able to produce a beam with lower energy spread ($\Delta E \approx 0.5$ eV) and higher brightness, which is important in regard to aberrations

and spectroscopy, as discussed later. The electron source has to stay in ultra high vacuum (at least 10^{-8} mbar) to avoid interaction between beam electrons and ambient gas molecules as well as to keep the tungsten tip and the anodes free from contamination. Additionally the tip has to be cleaned periodically by heating it shortly to remove any contamination that was absorbed on its surface.

Electron lenses

Like in light microscopy lenses are used for shaping the probe beam. This analogy holds for most basic lens equations like the calculation of focal lengths and magnification. Unlike photons in light microscopy, high energy electrons in STEM have a mass, a charge and a much shorter wavelength. Therefore strong electric or magnetic fields are needed to change their trajectories. In STEM, electric potentials are used to extract electrons from the source while magnetic fields are used to shape and focus the beam. The electric $\vec{E}$ and magnetic fields $\vec{B}$ interact with charged particles according to the Lorentz force

$$\vec{F} = -q(\vec{E} + \vec{v} \times \vec{B}) \ , \tag{3.8}$$

where q is the charge and $\vec{v}$ the velocity of the particle. Looking at the second part of the equation, we see that the force affecting the beam electron is perpendicular to the magnetic field and the velocity vector which leads to a circular motion around the optical axis. If the electron travels along the magnetic field lines it is not effected by the Lorentz force, which is the case for electrons along the central optical axis. As the local magnetic field strength of the typically rotational symmetric coils depends on the distance to the optical axis, electrons further away from the axis experience a stronger force. This leads to a helical inward motion leading to the focusing effect of the electromagnetic lenses. A change in the current that runs through the coils is followed by a change in the magnetic field, consequently altering the force acting on the electrons and the focal length of the lens.

Lens aberrations

The resolution of a microscope is not only limited by the Abbe diffraction limit (see equation 3.1) but also by practical limitations, most notably lens aberrations inherent to optical systems. In light microscopy glass lenses can be precisely manufactured in a way that aberrations become negligible whereby the resolution is limited by the wavelength. In electron microscopy the aberrations are the limiting factor and a complex system of electron lenses has to be implemented to achieve atomic

resolution. In the following the four most important aberrations, namely chromatic, spherical, comatic aberration and astigmatism will be briefly discussed.

As can be seen in equation 3.8 electrons with different velocities (thus different kinetic energies) are influenced differently by the magnetic lenses which leads to imprecise focus lengths if the primary electron beam has a significant energy spread (in other words if the primary electron beam is not monochromatic). This effect is called chromatic aberration and can be corrected by installing a monochromator after the electron source [74]. Although the Nion UltraSTEM 100 does not have a monochromator the energy spread of the cold field emission gun is small enough ($\Delta E \approx 0.5$ eV) for the chromatic aberrations to not be the main limiting factor.

As the primary beam has a finite diameter, some electrons are located further away from the central optical axis then others. As the magnetic field strength depends on the distance to the optical axis, these electrons are over-focused and hit different spots on the sample, blurring out the image. This is called spherical aberration.

Astigmatism is caused by the fact that the pole pieces of the magnetic lenses cannot be manufactured perfectly, thus breaking the symmetry of the magnetic fields. This results in a slightly different change in the electron trajectories depending on the azimuthal angle.

Comatic aberrations arise from electrons being focused differently depending on their incoming angle relative to the optical axis.

Already in 1935 Scherzer proposed that spherical aberrations are intrinsic to electron lenses as long as the following conditions are true [75]:

1. The fields are axially symmetric
2. There are no space charges
3. The fields are time-independent

While the other types of aberrations are in principle fixable, the spherical aberration can only be corrected if one of those conditions is broken. To achieve this, aberration correction methods use multipole lenses creating non-axially symmetric fields. In the case of the Nion UltraSTEM 100 this is done by a combination of four quadrupole and three octopole lenses which correct the aberrations of the other lenses. In order to find the right magnetic field strengths of the respective magnetic lenses, first the aberrations of the beam have to be measured. This is done

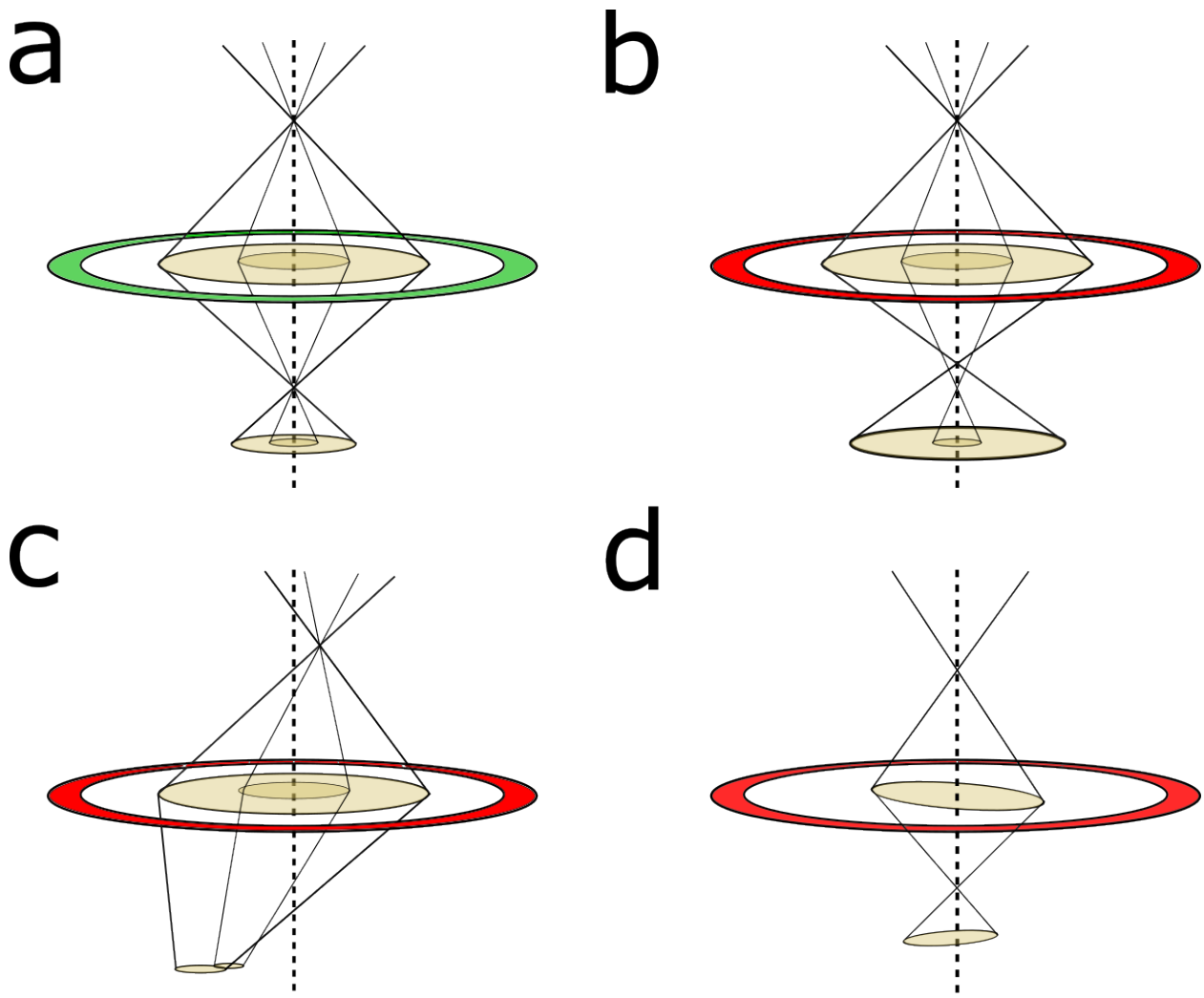

Figure 3.3: Schematic illustration of different lens aberrations in STEM. a) Aberration-free convergent beam. b) Spherical aberration. c) Comatic aberration. d) Astigmatism. Based on an illustration by Daniel Scheinecker [77].

by the AutoSTEM X algorithm which shifts the beam in a well-defined pattern on a spot of the sample without a clear crystalline order and collects the images using the Ronchigram camera. In every iteration the algorithm calculates the local distortions and tunes the lenses accordingly to correct the beam aberrations (see [76] for a more detailed description).

3.1.7 Detectors

One of the strengths of STEM imaging is the possibility to use many detectors at the same time. For example, it is possible to do electron energy-loss spectroscopy while imaging the area simultaneously. The main detectors of the Nion UltraSTEM 100 are the CCD detector (Ronchigram camera) and the ADF detectors. The Ronchigram camera acquires digital images of a lumines-

cent film hit by the scattered and unscattered electrons. It is mainly used for sample-navigation and to tune the set-up using the AutoSTEM X algorithm. In this thesis it is also used to collect convergent beam electron diffraction patterns.

ADF detectors have a ring-like shape and collect electrons, which are scattered within an angular range of $\theta_{min} < \theta_0 < \theta_{max}$. The intensities detected by the ADF detector are the integrated scattered intensities at each probe position. As the scattering intensity depends on the strength of the Coulomb interaction, which correlates with the atomic number Z, scattering on higher Z atoms is enhanced which leads to higher contrast, so called Z-contrast. The resulting contrast difference between atoms with higher and lower atomic number allows a straightforward analysis of the atomic structure and the identification of defects and impurities. In the high angle annular dark field (HAADF) detectors electrons are detected between $\theta_{min} = 80$ mrad and $\theta_{max} = 300$ mrad. It is well suited to analyse structures made of heavy atoms ($Z \geq 10$) with the scattering intensity being proportional to $Z^{1.64}$ [76]. In medium angle annular dark field (MAADF) detectors electrons with scattering angles between $\theta_{min} = 60$ mrad and $\theta_{max} = 200$ mrad are detected. This is beneficial for imaging of lighter atoms (e.g. carbon) but in thicker specimen the direct Z-contrast of HAADF is lost due to multiple scattering and interference effects, which makes the images harder to interpret. Both, HAADF and MAADF detectors work on the basis of a scintillator-photomultiplier combination. The scintillator emits photons when it gets hit by electrons. This signal gets amplified by the photomultiplier and is then converted into an electrical signal. This setup allows fast and efficient detection of scattered electrons, which is a requirement for atomic scale STEM imaging.

3.1.8 Electron energy loss spectroscopy

STEM EELS uses inelastically scattered electrons to obtain information about the elemental composition and the chemical bonding at the atomic scale. Electrons traveling through the center hole of the ADF detectors are dispersed with a magnetic prism based on their kinetic energy and recorded to form a spectrum. Electrons traveling through the prism experience the Lorentz force (see equation 3.8) and the centripetal force

$$\vec{F} = \frac{m\vec{v}^2}{R} \,. \tag{3.9}$$

where F is the force, v the velocity of the electron and R the radius of the circular trajectory. Equating both forces and assuming that the constant magnetic field is perpendicular to the velocity vector yields

$$R = \frac{mv}{qB} \, . \tag{3.10}$$

As all electrons have the same mass and charge and experience the same field strength, the radius only depends on their velocity and therefore on their kinetic energy. Electrons with different energies hit the fluorescent screen at the end of the prism at different positions creating a spectrum (see figure 3.4). To get a useful spectrum without measuring at a location for too long, a specific part of the spectrum can be selected by shifting the beam up and down.

The specific transitions corresponding to the excitation of inner shell electrons give rise to so called ionization edges. These features are considered to be in the high-energy loss region of the EELS spectrum, which starts at around 50 eV and extends to several thousand eV. Information about the chemical bonding of the atoms can be found in the fine structure of the ionization edges. Peaks associated with plasmon and phonon excitations can be found in the lower loss region below 10 eV. By comparing the measured spectra with EELS database spectra (e.g. the "EELS atlas" [78]), the ionization edges can be used for a qualitative identification of atomic species.

The spatial resolution of STEM EELS is limited by the probe size and the cross section of the respective excitations. By recording a spectrum at every pixel and putting them together into an image, elemental composition maps can be recorded, which offer additional insight into the mesoscopical structure of the material. The energy resolution of the spectrum is limited by the energy spread of the electron source and the quality of the EELS spectrometer. The energy spread of the Nion UltraSTEM 100 is in the range of 0.5 eV, which is good enough for elemental identification but does not allow for the resolution of subtle fine structures. Electrons which pass the sample without interacting make up the zero loss peak, which has a certain width due to the energy spread of the electron beam, creating a background over the spectrum. Also the detector itself contributes to the background. To gather exact quantitative information about the spectrum, the background around the ionization edges has to be fitted using a power law formula and subtracted from the signal.

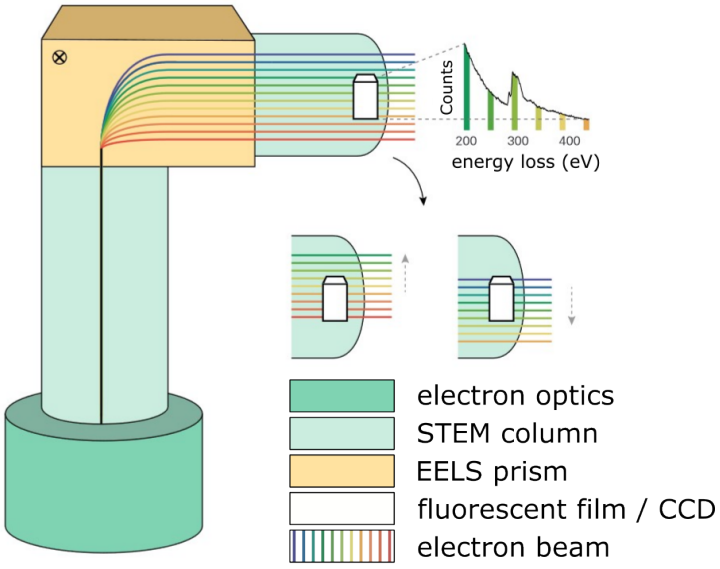

Figure 3.4: Schematic illustration of an EELS setup. The electrons are split by a magnetic field according to their energies (spectral colors). A certain part of the energy spectrum can be selected by decreasing the magnet's strength, thus moving the beam up or down. The selected range of the beam hits a fluorescent film, which is filmed by a CCD camera. The spectrum on the top right shows the carbon K edge of graphene. Illustration by Christina Schmolmüller with permission of the author.

3.1.9 Convergent beam electron diffraction

Electron diffraction is a technique based on elastic electron scattering that allows determination of the crystal structure of materials. In a simple description (derivation from [79]) the electron is described as a spherical wave $\Psi = e^{ikr}$ with wavevector $k = 1/\lambda$ that diffracts at a sum of atomic potentials $\sum_R V(r' - R)$ (e.g. the crystal lattice of a material) yielding

$$\Psi_s(r, \Delta k) = -\frac{m_0}{2\pi\hbar^2}\frac{e^{ikr}}{r}\int \sum_{R_i} V(r' - R_i)e^{-i\Delta k r'} d^3r' \tag{3.11}$$

.

Where m_0 is the electron mass, $\hbar$ the reduced Planck constant, R_i the atomic positions and $\Delta\vec{k} = \vec{k} - \vec{k_0}$ is the change of the wavevector after scattering (note $|\vec{k_0}| = |\vec{k}|$ because no energy is lost in elastic scattering). By substituting $r' = r - R_i$ the spherical wave can be dropped to get

$$\Psi_s(\Delta k) = \sum_{R_i} f(R_i, \Delta k)e^{-i\Delta k r_i} \quad and \quad f(R_i, \Delta k) = -\frac{m_e}{2\pi\hbar^2}\int V_{R_i}(r)e^{-i\Delta k r} d^3r \ . \tag{3.12}$$

$f(R_i, \Delta\vec{k})$ is the form factor of an individual atom at site R_i. The structure of a crystal can be described by the sum of its lattice structure (one of the 14 Bravais lattices) plus a basis $R = r_l + r_b$. By inserting this relation into equation 3.12 we get

$$S(\Delta k) = \sum_{r_l} e^{-i\Delta_k r_l}\sum_{r_l} f(r_b)e^{-i\Delta_k r_b} = S(r_l, \Delta_k)F(r_b, \Delta_k) \ , \tag{3.13}$$

where S is the crystal shape factor, associated with the lattice symmetry, and F the structure factor, depended on the basis. The scattering function in equation 3.12 has a maximum at

$$\Delta k R_i = 2\pi \cdot n \qquad \text{or} \qquad \Delta k = n \cdot g \ , \tag{3.14}$$

where n is an integer and $\vec{g}$ a reciprocal lattice vector of the crystal. This equation is called the Laue condition and gives the requirement for constructive interference in a diffraction experiment. A convenient way to visualize this relation between the reciprocal lattice and the scattered wavevector is the Ewald sphere (figure 3.5). Every time the Ewald sphere (radius $1/\lambda$) touches a reciprocal lattice vector in the so called Laue zone, the Laue condition is met and the constructive

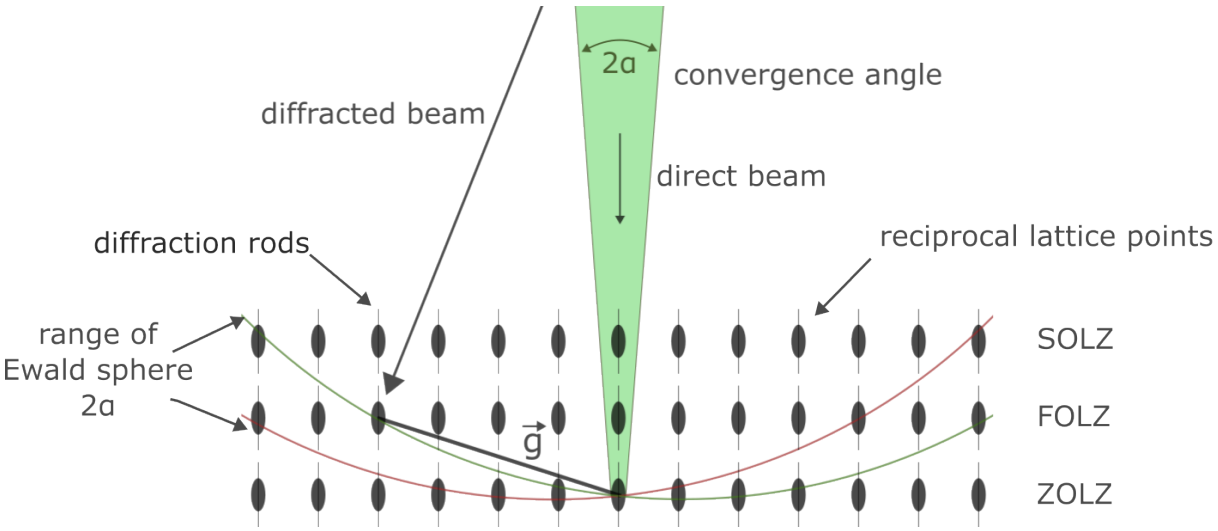

Figure 3.5: Schematic illustration of CBED. When the Ewald sphere touches a reciprocal lattice vector $\vec{g}$ in one of the Laue zones the Laue condition is met and a diffraction spot appears. Due to the convergence of the beam the Ewald sphere has a finite thickness (range between green and red sphere) and the reciprocal lattice points are extended to disks. Due to the finite sample thickness the diffraction points become rods. ZOLZ, FOLZ and SOLZ stand for zero-order, first-order and second order Laue zones, respectively. Note that this illustration is not up to scale. In reality the Ewald sphere is much larger in comparison to the reciprocal lattice rods. Based on an illustration by Toma Susi.

interference leads to a diffraction spot in the diffraction image. If the sphere misses a reciprocal lattice vector by a small error of $\vec{s} = \Delta\vec{k} - \vec{g}$ the diffraction spot will have less intensity. As can be seen in equation 3.12, the intensity of the diffraction spot is also determined by the form factor [79].

This theory describes the diffraction pattern of thick and mono-crystalline samples under a parallel irradiation. In samples with finite thickness D, the diffraction spots become rods with a diameter proportional to D. Poly-crystalline samples have a ring-like pattern which becomes continuous with smaller grain sizes [79].

When the electron beam is not parallel, but converges with a convergence angle α, like in the case of STEM, the small diameter of the beam opens up an angular range in reciprocal space and the Ewald sphere has a finite thickness. Thus the diffraction from higher order Laue zones becomes visible. In convergent beam electron diffraction (CBED) diffraction spots become disks, the broadness of these disks is proportional to the convergence angle [68].

CBED is a very convenient technique to obtain structural information of a STEM sample as it

allows to obtain diffraction images from very small areas and does not need additional instrumentation. It allows to measure for example lattice constants, grain boundaries, strain information or sample thickness [68].

3.2 Sample preparation

To achieve the ultimate goal of this thesis, the production of unoxidized monolayer BP samples, suitable for STEM characterization, special measures are needed. The exfoliation and transfer process has to happen inside an argon-filled glovebox and no liquids can be used to prepare the samples. Then the samples must be transferred into the STEM column without exposure to ambient conditions. The vacuum level during transfer, cleaning, storage and imaging should never exceed 10^{-6} mbar.

3.2.1 Exfoliation

The first step in the sample preparation is the mechanical exfoliation of a thin BP flake from a bulk crystal using the method developed by Novoselov and Geim [4]. A piece of the crystal is gently pressed against adhesive tape and peeled off leaving some of the material on the tape. Then the tape is repeatedly folded onto itself and peeled apart, thinning down the material. This procedure is repeated 3-4 times, as repeating it more often would lead to smaller lateral sizes of the flakes but not necessarily thinner flakes.

3.2.2 Transfer

Two methods have been tested to transfer a suitable BP flake from the adhesive tape onto a SiN transmission electron microscopy grid.

PPC transfer

The first transfer method, first described by Pizzocchero et al. [80] and modified by Kinoshita et al. [81], utilizes the thermoplasticity of a polypropylene carbonate (PPC) film on a polydimethylpolysiloxane (PDMS) substrate. Thermoplastic materials have a rigid surface below a

specific temperature but become soft at elevated temperatures. In the case of PPC there is strong adhesion between the PPC and low-dimensional materials (e.g. graphene, h-BN, BP) at room temperature, which is significantly lowered when PPC is heated up to 70°C. This property is used for a reliable pick-up and release of the materials.

The PDMS is produced by carefully mixing 1 part of elastomer with 10 parts of curing agent in a plastic petri dish for about 5 min. Subsequently the PDMS is dried for about 48 h at room temperature. One has to take care to not produce air bubbles in the PDMS before it dries. If such bubbles appear, they have to be removed by pumping them out using a small vacuum pump. Once the PDMS has dried it is cut into ca. 2×4 mm^2 pieces. The pieces (stamps) are put onto a glass slide and are plasma-cleaned for 10 minutes at 50 % power (50 W) under a pressure of $5 \cdot 10^{-1}$ mbar. Next the PPC is prepared by mixing 15 parts of anisole with 1 part of PPC and left under a fume hood for approximately 24 h. The next day a PDMS stamp is attached onto a spin-coating device using adhesive tape (the tape should not be too adhesive and should not leave any residue behind) and a small drop of the PPC-anisole mixture is put onto the stamp, which is then spin coated on the stamp for about 3 seconds at about $1400 - 1600$ RPM. Next a very small amount of super-glue is dropped on the edge of a clean glass slide and the spin coated stamp is placed on the glue so that a part of the stamp hangs over the edge of the slide as can be seen in figure 3.6a. During the whole process the stamp should be handled very carefully, as any blisters and wrinkles in the stamp lower the yield of the transfer process significantly.

A ca. 1 cm^2 sized piece of a SiO_2 wafer is plasma-cleaned for 10 min with 100 % power (100 W) and put into the glovebox, together with the prepared glass slide. Then the exfoliation tape with the BP is pressed softly onto the wafer and shortly heated to 70°C to improve material transfer. Once the tape is removed, one can search for thin layered areas using the optical microscope within the glovebox. Then the glass slide is mounted on the micro-manipulator and slightly bent towards the flake as can be seen in figure 3.6b. To begin the pick-up process, an edge of the stamp is brought right over the identified flake and the stamp is lowered until it completely covers the flake. The wafer is heated to 70°C for about 60 s, after which the stamp is lifted up steadily. Now the stamp should have picked up the material, which can be verified by checking the SiO_2 after the pick up. For the drop down process (figure 3.6c), a plasma-cleaned (100 W, 10 min) SiN grid is put into the dent in the middle of the microscope stage, where a vacuum tweezer is attached to hold the grid in its place. The stamp is moved into a position so that the flake is located directly over the middle of the SiN grid. The stamps is lowered until it attaches. The grid is heated to 110°C for about 3 min, then the stamp is picked up slowly, but steadily until it is

fully detached, while the heating stays at a constant 110°C. Now the flake should be transferred onto the grid.

This dry transfer technique is supposed to be clean, simple and applicable to a wide array of layered materials such as h-BN, graphene and MoS_2 [81]. In practice it took us a long time to adjust the parameters until a transfer of BP onto the SiN could be achieved. Even after a suitable set of parameters had been found, the method remained unreliable, time-comsuming and frustrating[1]. At least the following four parameters have to be optimized before the PPC method is reasonable for BP transfer:

1. PDMS plasma cleaning power and duration
2. type of adhesive tape for spin coating
3. pick-up and drop-down temperature and heating duration
4. velocity of the stamp during the drop-down process

It needs to be mentioned that a former student found suitable parameters for graphene transfer. Using his parameters the transfer of graphene could be reliable reproduced.

PDMS transfer

As the PPC transfer technique turns out to be unreliable, another method has to be used for sample production. After some trials, the viscoelastic PDMS transfer, first introduced by Castellanos-Gomez et al. [83], has been chosen as it does not need additional equipment and stands out as a very reliable, versatile and simple method. Viscoelastic materials behave like an elastic solid on short timescale (e.g., when peeled off rapidly from a substrate), but flow slowly on larger timescales (e.g., when peeled off very slowly). This behaviour leads to a kinetically controllable adhesion between the viscoelastic material and solid objects at its surface which can be used to reliable pick up 2D materials from one substrate and transfer it to another [84].
The PDMS used for this transfer method was bought commercially (Gel-Film© WF ×4 6.0mil). The main advantage of this Gel-Film© over in-house produced PDMS is its superior flatness which makes the transfer process easier. The Gel-Film© comes with two layers of protection, which both

[1]Interestingly, the poor reproducibility of the PPC transfer method has been an example in a 2023 publication about the reproducibility gap in graphene research [82].

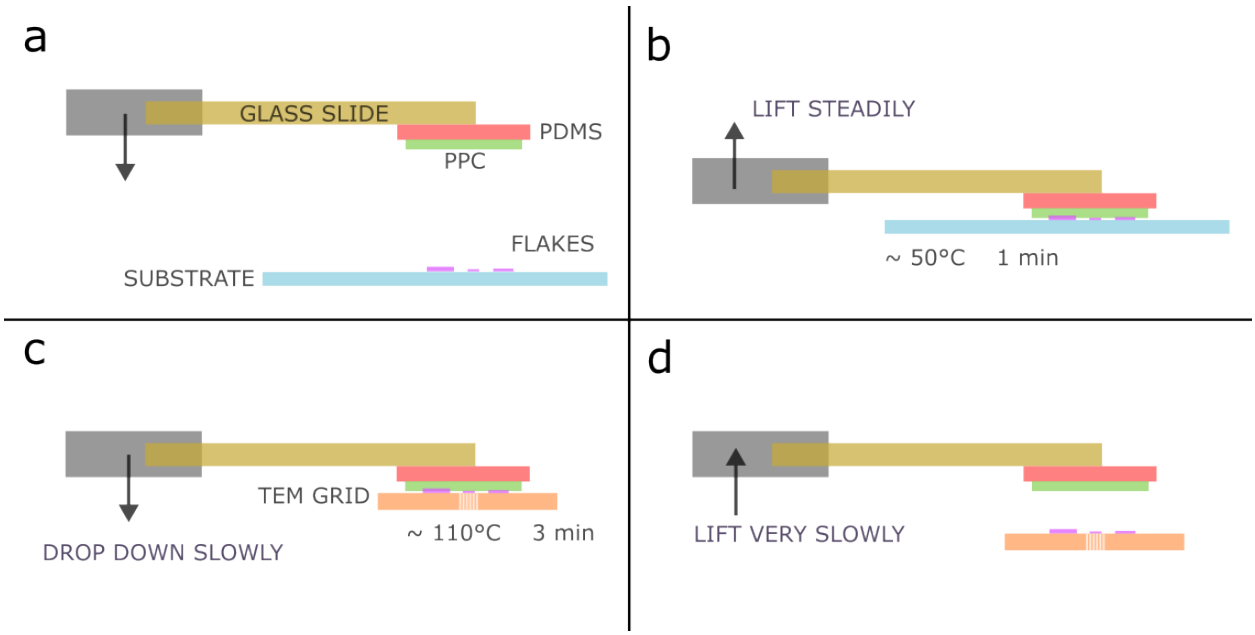

Figure 3.6: Schematic of the PPC dry transfer method. a) The PDMS/PPC stamp is glued onto the edge of a glass slide and held in place with the micro-manipulator. b) The stamp is placed on the flake and heated up to 50°C for about 1 min. Then the stamp is lifted up steadily. c) The stamp with the material is placed on the SiN grid and heated to 110°C for 3 min. d) The stamp is lifted very slowly to transfer it onto the TEM grid.

have to be removed carefully before dropping the stamp of ca. 4x8 mm^2 close to the edge of a clean glass slide. Afterwards the glass slide is put into the glovebox. The material-loaded tape is pressed softly against the stamp and peeled off. To produce thin flakes this may be repeated a few times. A large piece of SiO_2 wafer is put on the stage of the visible light microscope, to act as a mirror for reflection mode light microscopy. Then the glass slide with the stamp is placed on the wafer and can be scanned for suitable areas. BP appears very colorful under the optical microscope; bulk areas appear black, whereas thin areas appear green and yellow (see figure 3.7a-b). A monolayer of BP is supposed to have an optical absorption of about 3.3 percent [15], thus atomically thin flakes will have nearly the same colour as the blueish reflection from the SiO_2 mirror and monolayers would not be distinguishable using the available equipment. Using this method it is only rarely possible to exfoliate isolated thin flakes and reasonably thin areas will always attach to bulky, yellowish-green areas. Switching to the green channel makes identification easier.

Once the desired flake has been found, the glass slide is rotated by 180° and mounted onto the micro-manipulator. A plasma-cleaned SiN grid is put in the dent on the microscope stage and the vacuum tweezer is attached. The stamp is brought to a position right above the grid. Now the

microscope stage is lowered a bit to put the grid in a slight overfocus (note that the focal length changes due to the refractive index of the PDMS stamp). The glass slide is lowered very slowly to reach the focus plane of the material on the bottom side of the stamp. Once the chosen flake is brought directly above the grid, the glass slide is raised again and the grid is brought back into focus (figure 3.7c). Now the stamp is lowered very slowly (in the order of a few minutes) until it attaches to the grid. When the PDMS gets into contact with the grid, the colour in the attached areas changes (figure 3.7d). The slide is lowered until slightly more than the desired flake is attached to the grid. Now the stamp is raised very, very slowly to lower the adhesion between the material and the stamp, while maintaining the high adhesion between the grid and the material (figure 3.7e). It is important to maintain the slow speed even after the attached area has moved out of the field of view as an increased speed bears the risk of the grid clinging onto the stamp. Once the stamp has completely detached it can be removed from the micro-manipulator to be reused.

3.2.3 BP-graphene heterostructures

To produce BP-graphene heterostructures (from now on called BP/G), graphene has to be transferred onto the SiN grid. Although it would be possible to simply put BP on dry-transferred graphene flakes, exfoliated from HOPG, it is more convenient and reliable to put BP on commercial CVD-grown Graphenea© easy-transfer graphene, which was transferred to the grid beforehand. Easy-transfer graphene consists out of three layers, the graphene being sandwiched between a sacrificial layer and a polymer film. A small piece of it is cut out and slowly immersed into deionized water to remove the polymer film. After the sacrificial layer/graphene film is detached from the support it will float freely in the water. Using inverted tweezers the SiN grid is introduced into the water and lifted to scoop up the floating film from below. After inspection in a light microscope the sample is annealed at 150°C for 1 h. Afterwards the sample is dipped into acetone residing on a hot plate at 100°C for 1.5 h to remove the sacrificial layer. Then the grid is immersed into IPA for 1 h. Because a monolayer of graphene on SiN is not visible in light microscopy, the presence and cleanness of graphene over a certain window is confirmed by Raman spectroscopy[2]. The finished graphene on SiN samples are put into the glovebox where they are

[2]The G peak at ca. 1580 cm^{-1} and the D peak at ca. 1340 cm^{-1} in the Raman spectrum are indicators for the presence of graphene and the presence of defects, respectively. The D/G peak ratio is a measure for the defect concentration in the sample, the appearance of broad features around D, G and the second order 2D peak is a indicator for large amounts of contamination [85].

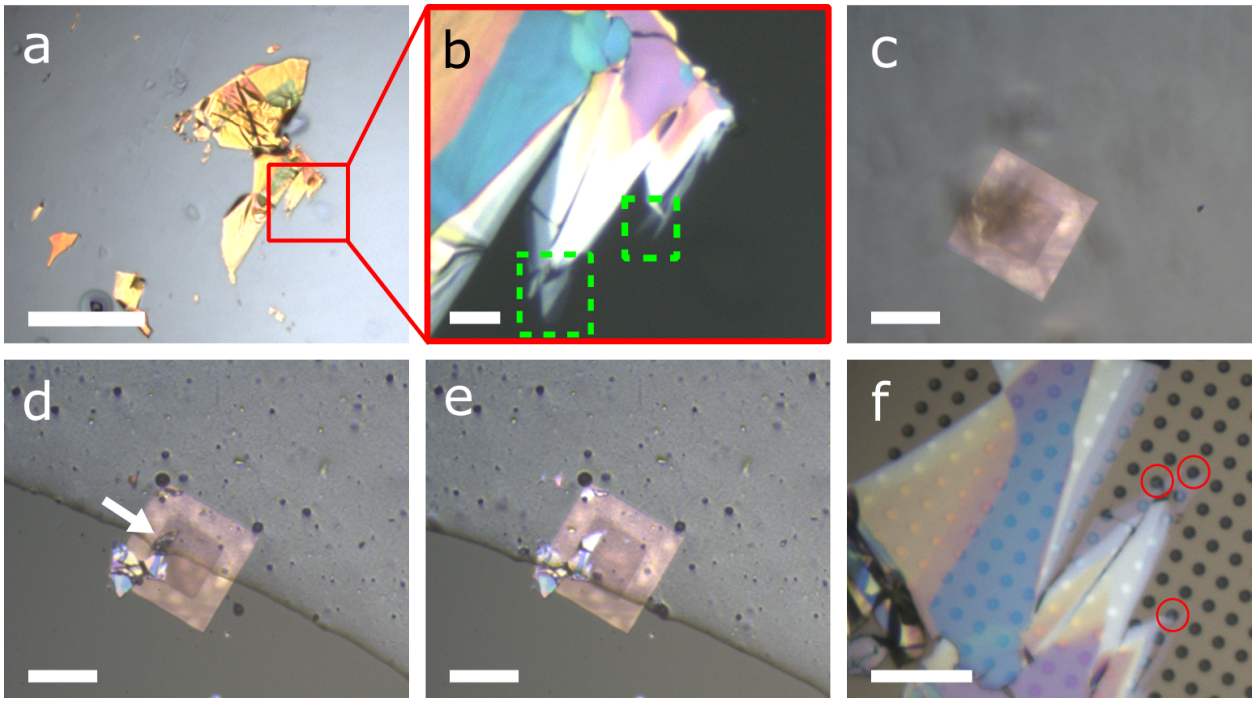

Figure 3.7: The PDMS dry transfer technique. a) A typical BP flake after exfoliation on the PDMS stamp seen with 5x magnification. The dark spots inside the flake are bulk areas. The greyish dots are probably dirt particles enclosed between the glass slide and the PDMS. b) The red squared area of the flake depicted in panel a with 50x magnification. The thin areas on the lower side of the flake (green squares) are approximately 5-7 layers thick. The thickness has been estimated by counting the number of removed layers when drilling a hole with the STEM electron beam. c) The SiN TEM grid seen through the glass slide with the BP on the PDMS stamp slightly out of focus. d) After lowering the glass slide the PDMS stamp has attached to the grid. Most of the flake is in contact with the grid, only the top corner of the flake is still hanging over the grid as indicated by the black color (white arrow). e) After the whole flake is attached to the grid, the glass slide is raised very slowly. The whole material sticks on the grid as indicated by the color of the BP. f) The BP on the grid after the transfer. The thinnest flakes are barely visible in the light microscope (holes marked in red). Scale bars 100 µm (a), 10 µm (b), 250 µm (c-e), 20 µm (f)

annealed at 350°C for 1 hour to remove residual oxygen and other contaminations. Now BP can be transferred onto the graphene as already described. Irradiating the graphene for 40 min with a 445 nm laser under UHV conditions using a power of 27 percent (1.62 W) would further improve cleanness [86].

3.3 The CANVAS system

After the samples are fabricated they are introduced into the CANVAS ultra-high vacuum (UHV) system (CANVAS stands for "controlled alteration of nanomaterials in vacuum down to the atomic scale") [21]. It consists of an array of vacuum pipes connecting manipulation and measurement devices. To move samples between different sites, sample holders ("pucks") are loaded into "cars" that can be moved inside the pipes by hand using magnets. The samples are introduced via the loadlock which is directly connected to the glovebox. After introduction the samples are baked at a temperature of ca. 160°C for a few hours to remove contamination on the grids, the "cars" and the "pucks". The samples can be stored in one of two storages or be altered in the "target-chamber". Possible methods of sample-manipulation are e-beam evaporation, thermal evaporation, plasma irradiation or illumination with a 445 nm laser (maximal power 6 W). Additionally they can be imaged using a GETec© AFSEM atomic force microscope. The main instrument of the CANVAS system is the aberration-corrected UHV scanning transmission electron microscope Nion UltraSTEM 100. Typical pressures inside the UHV system are 10^{-6} mbar in the loadlock, $10^{-7} - 10^{-9}$ mbar in the connecting pipes and in the storage chambers and 10^{-10} mbar inside the STEM column. Figure 3.8 shows a schematic illustration of the CANVAS system with photographs of the most important parts.

The Nion UltraSTEM 100 (figure 3.2b) is equipped with a 3rd generation C3/C5 aberration corrector and operates with electron energies between 55 eV to 100 eV. The electrons are emitted from a 100 kV cold field emission gun located at the bottom of the instrument. Through an array of lenses the aberrations are corrected to bring the probe size down to 1 Å to reach atomic resolution. The electrons are detected either via a MAADF detector with a detection range of 50-200 mrad or with a HAADF detector with a range between 80 and 300 mrad. The instrument is equipped with a PEEL© 666 spectrometer from Gatan to perform EELS and a 473 nm pulsed laser with a spot size of ca. 40×45 µm^2. Two modifications set this microscope apart from similar devices: Firstly it is directly connected to the CANVAS UHV system using a custom made stage

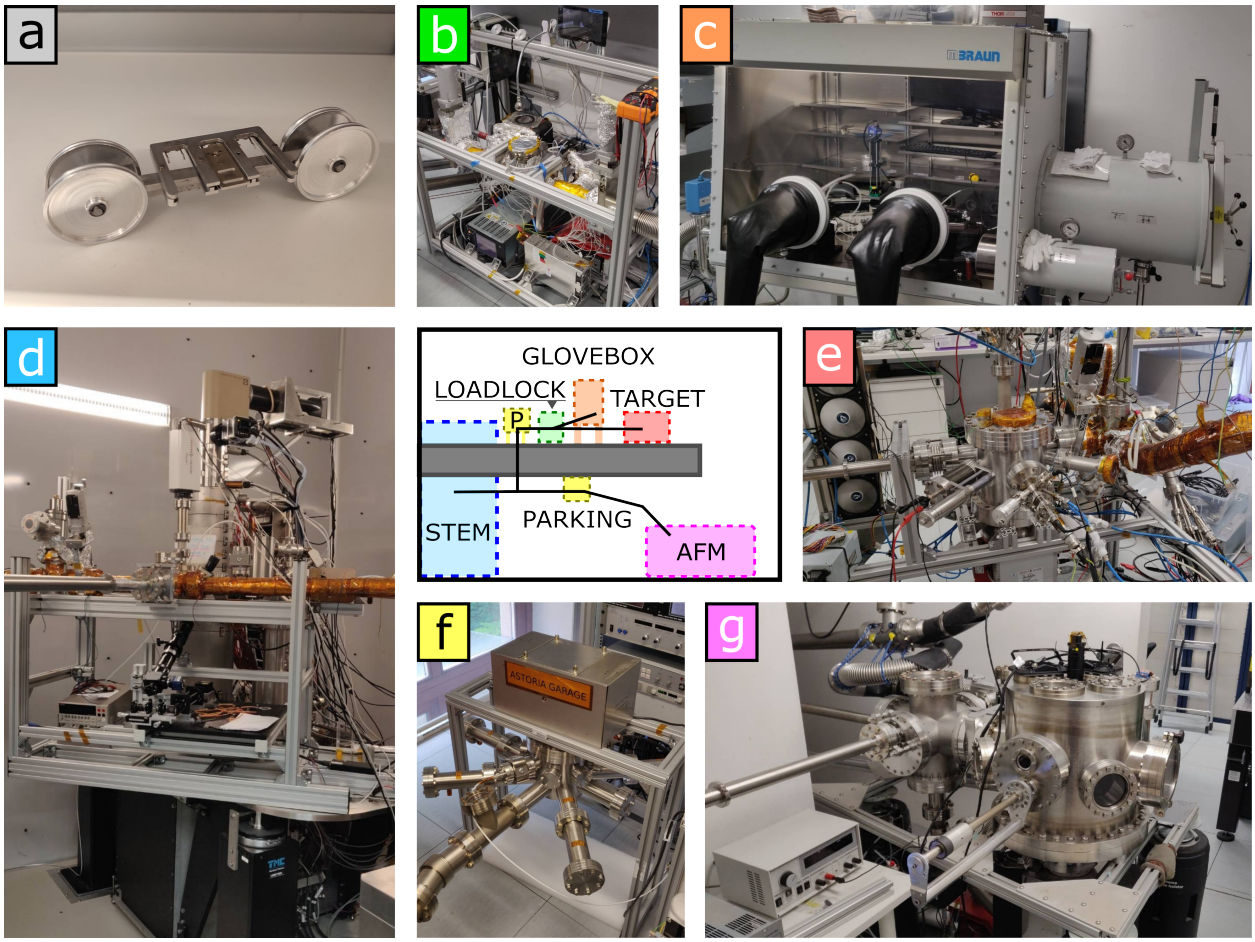

Figure 3.8: Center: Schematic depiction of the CANVAS system. a) A "car" with a sample holder "puck" inserted in the middle slot. b) The loadlock used to introduce samples into CANVAS. c) The MBraun© LABstar glovebox. d) Nion UltraSTEM 100 with laser setup and connection to the CANVAS system e) The target-chamber with a variety of sample-manipulation devices. f) One of the two sample storages. g) Chamber for the GETec© AFSEM microscope. Photo courtesy b-g by Carsten Speckmann.

and sample insertion system. The second modification is a gas line with a leak valve, allowing the introduction of gases like H_2O or O_2 in precisely controlled quantities to achieve partial gas pressures of up to 10^{-6} mbar.

3.3.1 Glovebox and transfer system

The LABstar glovebox from MBraun© is installed at the first floor of the laboratory at Sternwarte. The left side wall has been removed and replaced by a custom made wall featuring three ports as can be seen in figure 3.9c. The front port is connected to a pipe of the CANVAS system. The second port is currently unused while the third port has an inlet for different gasses. The glovebox is fed with the working gas (argon) via a steel pipe on the backside. It features a gas cleaning system consisting of a side channel blower which pumps the working gas through a series of treatment devices to remove residue gases, specifically water and oxygen. The argon is kept at a slight overpressure of approximately 2 mbar so that microscopic leaks are mostly leaking the working gas out of the box instead of letting ambient gases in. The partial pressure of oxygen and water is observed by calibrated sensors and should always stay below 1 ppm. Samples and working material can be introduced into the glovebox using one of the two airlocks mounted on the right side wall.

At the start of this thesis project the glovebox was heavily leaking, losing all its overpressure in a few minutes and the gas cleaning system did not work properly. After failed attempts to find the leak using conventional leakage spray, the left side wall was disassembled and re-insulated, to no success. Dichlordifluormethane gas (also called Freon-12) was finally introduced via the side-wall inlet to identify the leak. Freon escaping from the glovebox has been detected using a commercial HCFC sensor and a major leak has been identified at the feed-through of the right glove. After dismantling and reinserting the feed-through the loss of overpressure stopped although smaller leaks at both sidewalls remained. Subsequently the problem with the gas cleaning system has been solved by replacing its defect side channel blower. After the system was repaired, the filters had to be cleaned by purging the glovebox. In this process the glovebox is heated up and varigon gas (95 percent argon, 5 percent hydrogen) is introduced. The hydrogen reacts with the oxygen in the filter, creating water vapor, which is removed by the gas pumps of the purging system.

The transfer system inside the glovebox has been constructed by a former student and consists of a microscope, a separately movable heating stage and a xyz micro-manipulator for the glass slides. All of these parts are mounted on a breadboard via adjustable rails. The microscope has a

Figure 3.9: Photographs of the glovebox at Sternwarte laboratory. Image a) shows the inside. The microscope setup, a computer with screen, mouse and keyboard, the heating stage as well as power supplies, the vacuum tweezer and sample storages are visible. Image b) shows the glovebox next to the loadlock part of the CANVAS system, the loadlock in the front and the up-stairs sample "garage" in the back. Image c) shows the custom made sidewall with the three ports. The port on the right side can be connected with the loadlock. The blue boxes connected to the steel pipe are the detectors of the gas cleaning system. Photo courtesy by Felix Herterich.

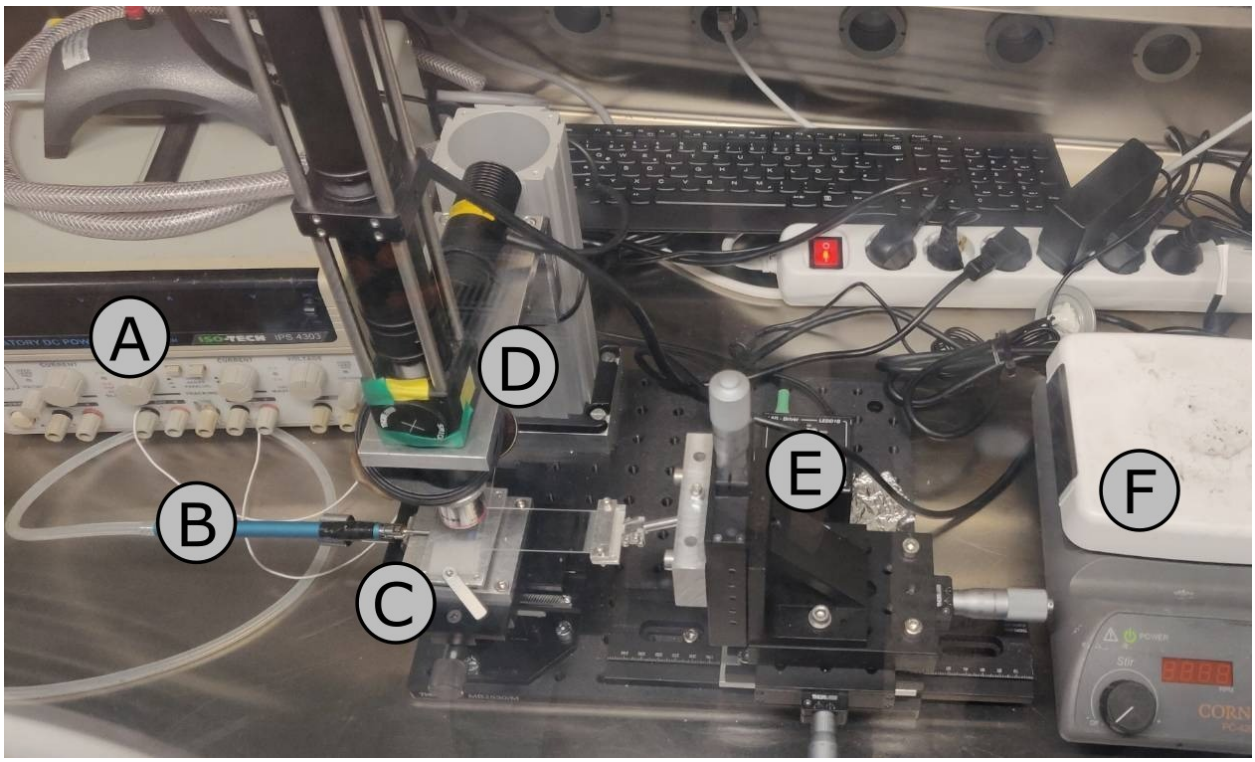

Figure 3.10: Photograph of the microscope and transfer setup. a) The power supply for the heating stage b) The vacuum tweezers attached at the microscope stage. c) The xyz microscope stage with the heating plate on top. d) The optical tube with the CCD camera on the far end and the illumination system feeding into the microscope. e) The micromanipulator with the glass slide holder and a mounted glass slide. g) Hot plate used to heat samples up to 500°C.

optical tube turret with a CCD camera on top and three objectives (4x, 10x and 50x) mounted on an objective revolver on the lower end. A light emitting diode in combination with an aspherical condenser lens is used to illuminate the sample uniformly. The heating stage is located directly below the microscope and consists of a xy positioning stage mounted on top of a vertical stage, all of which can be adjusted by screws. On top of the stages an aluminum plate on pedestals with a heating mat enables voltage-controlled heating of the samples up to 120°C. Additionally there is a socket on the aluminum plate which has two small holes where a vacuum tweezer can be attached to hold the SiN grids in place. The micro-manipulator is a preconfigured xyz stage with an adapter to connect different holders, e.g. the custom made glass slide holder for the PDMS dry transfer. The micro-manipulator is mounted on a rail to easily move it away and free up space when it is not needed.

3.3.2 UHV-annealing device

The best documented method to clean BP surfaces is annealing under UHV conditions. For example, Lee et al. [17]put BP samples into an electrical sample holder and heated them to temperatures between 220°C and 270°C directly in the STEM column. Although it is possible to insert similar heatable sample holders into the Nion UltraSTEM 100 they must be introduced via the original cartridge system which is not directly connected to the CANVAS system and using cartridges would expose samples to ambient conditions during the transfer. Alternatively, one may use so called electrical pucks which can be loaded into cars and handled inside the CANVAS system. These electrical pucks can be contacted inside the STEM column using the electrodes of a not fully inserted electrical cartridge and enable annealing of samples directly in the column. As this system is still in development and was not available at the time of the thesis, another method had to be implemented to clean the BP surfaces.

The UHV-annealing system specifically designed for this thesis consists of a 3D-printed aluminium-oxide (aloxide) oven inside a stainless steel frame (see figure 3.11). The oven is heated by a V-shaped tungsten filament from the company Kurt J. Lesker. It is introduced from the backside via a slit in the aloxide structure. The tip of the wire is located slightly off the line of sight to the sample to ensure that the sample is heated up efficiently without being exposed to material released from the hot wire. To measure the local temperature at the sample, a S-type thermocouple INCONEL-600 (Platinum/Rhodium 90/10% - Platinum 100%) covered by a PtRh tube is introduced through a hole in the back. It enables accurate measurement of temperatures up to 1600°C. Aloxide has been used as the primary material for the oven due to its high melting point of (above 2000°C [87]) and its electrical isolating properties. Former experiments with similar annealing devices showed that aloxide can become brittle when handled with conventional manufacturing tools like drills and milling machines, so we decided to 3D print the oven using the very recently developed "Lithography-based Ceramic Manufacturing" method in cooperation with the company Lithoz Gmbh [88]. The steel-frame was manufactured by the faculty workshop.

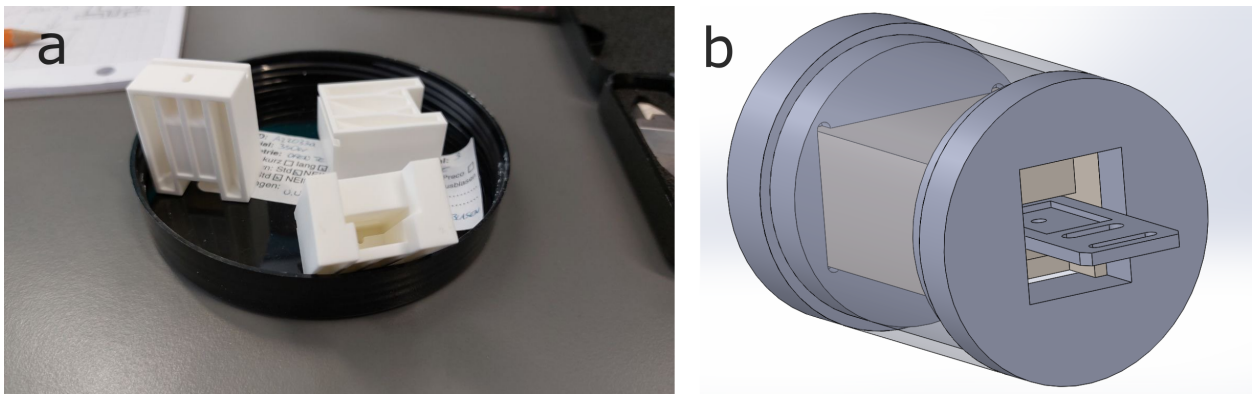

Figure 3.11: a) Photograph of the 3D printed aloxide oven as delivered by the company Lithoz Gmbh. b) A SolidWorks© sketch of the full assembly with a half-inserted puck.

Chapter 4

Results and Discussion

All electron microscopy images were taken with the Nion UltraSTEM 100 located in the Sternwarte laboratory at the University of Vienna. The light microscopy images were taken with the optical microscope inside the glovebox.

4.1 Phosphorene imaging

After the BP sample was prepared in the glovebox as described in section 3.2.2 it was introduced into the Nion UltraSTEM 100. Figure 4.1a shows a BP sample under the optical microscope with a thin layered piece adjacent to the bulk BP in the center of the figure. An overview image recorded by the Ronchigram camera in figure 4.1b shows a few partially covered holes next to a thicker area. At the first inspection it became clear that the sample is heavily contaminated with hydrocarbons appearing bright in the dark field images (see figure 4.1c), an observation which is already reported by various groups [13, 15]. Figure 4.1d shows the fast Fourier transformation (FFT) of the picture with FFT spots commonly associated with BP [11]. After we found a partially clean area with a size of ca. 2 nm^2 the area was imaged using HAADF for 17 min. In figure 4.2 the area is shown at the beginning of the measurement, after 2 min, after 4 min, after 8 min, after 10 min, after 12 min, after 15 min and after 17 min of irradiation. This image series shows layer-by-layer thinning of the multilayered BP sample. The first defects started to appear after about 1 min of irradiation. After 2 min (image 4.2b) the first layer began to disintegrate and after about 4 min the uppermost layer was fully removed. Figures 4.2d to 4.2f show the removal of the next three layers. In figure 4.2g the lattice begins to disintegrate in a contaminated

area in the bottom left corner of the image and after 15 min the first pore appeared. Figure 4.2h shows the pore growing over the clean area. Most notably the contaminated area remains nearly unaffected. The pore growth stops at the edges to the contamination. The observed layer-by-layer etching behaviour is in agreement with similar experiments reported in literature [15].

At atomic resolution, it is possible to estimate the layer number by looking at the stacking order. BP layers stack in the AB stacking order where every other layer is shifted by half a unit cell along the [100] ZZ direction. Thus the uppermost atoms of the lower layer can be seen in the spaces between the atoms of the upper layer. In the case of three-layer BP, this leads to a chess-board like pattern in the top down view [001] as has been reported by Wu et al [11]. BP can also stack in the AB' stacking order which looks identical in the top down [001] view because it is a 0.5 unit cell shift in the crystallographic direction [110] starting from AB stacking. Nevertheless AB stacking can be assumed, because the AB'-AB translation energy barrier is very low, which means AB stacking will be the stable stacking order at finite temperatures [11]. Figure 4.3 shows an experimental example of the AB stacking order in [001] direction next to calculated models for different stacking orders along the [001] crystallographic direction by Wu et al [11]. Using the stacking order as an indicator for three-layer BP we observe that very often the first pores appeared before the BP was thinned down to a monolayer. Usually the thinnest layers that could be observed for a reasonable number of frames were double- or three-layers.

Electron beam induced damage during STEM imaging can be attributed to knock-on damage, radiolysis and chemical etching. As already described in section 3.1.5 the maximum transferable energy from a 60 keV electron to a phosphorous atom is slightly below the calculated displacement threshold of 6 eV [71]. As the STEM operates at room temperature, the phosphorus atoms can not be described as static, thus equation 3.7 has to be applied. The atomic vibrations can be described via the statistical distribution of out-of-plane velocities. The mean square width of this distribution at a temperature T can be estimated using the Debye model [70] as

$$\overline{v^2} = \frac{3k_B\theta_D}{8M} + \frac{3k_BT}{M}\left(\frac{T}{\theta_D}\right)^3 \int_0^{\frac{T}{\theta_D}} \frac{x^3}{e^x - 1} dx \,, \tag{4.1}$$

where M is the mass of the phosphorus atom, k_B the Boltzmann constant and θ_D the Debye temperature. Using a Debye temperature for BP of 278.66 K [90] and the room temperature T = 293 K, we get a mean square width of the velocity distribution of $\overline{v^2} \approx 286.6$ m^2/s^2. Applying this number in equation 3.7 we can see that a significant amount of electrons can transfer energies

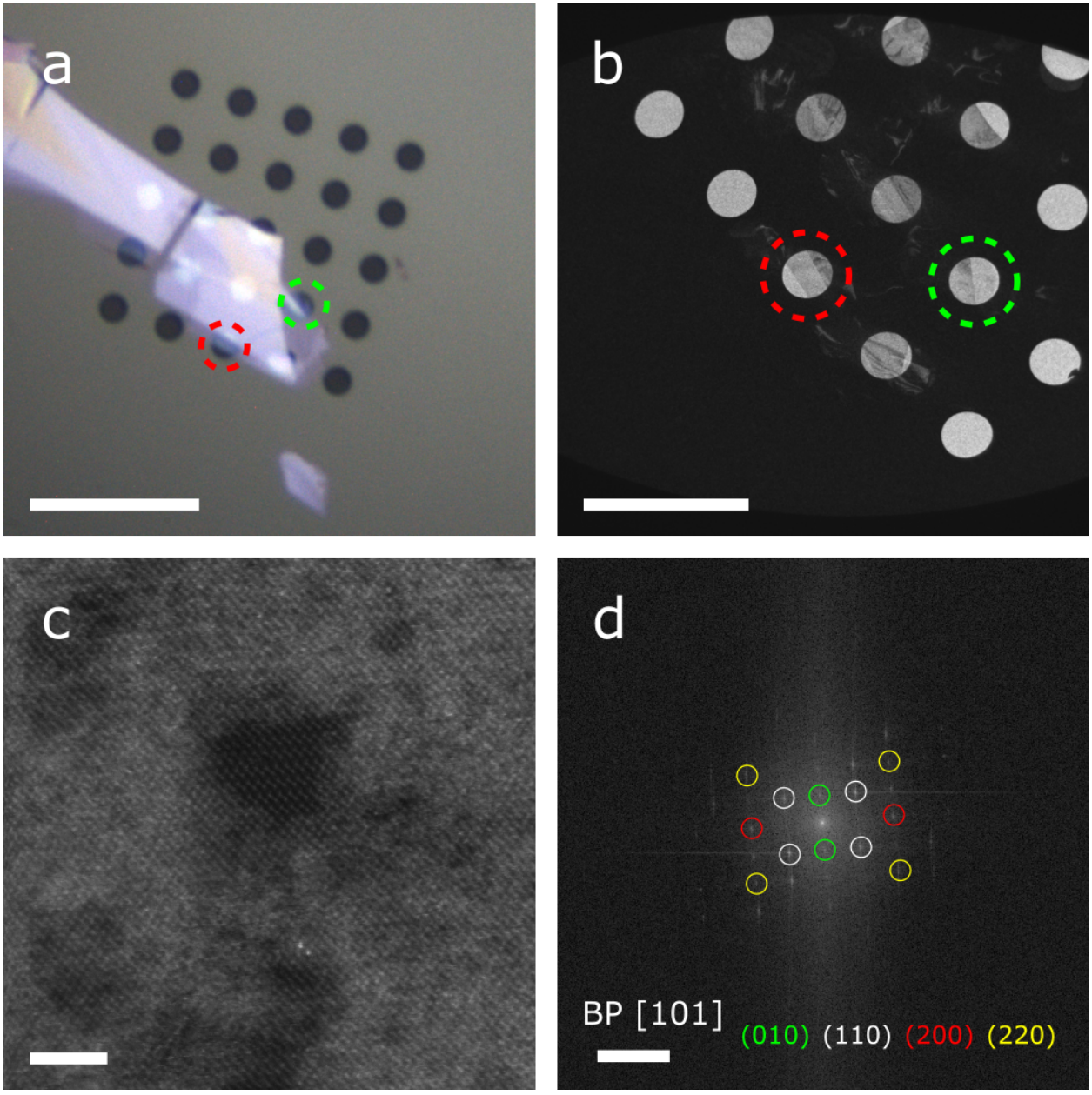

Figure 4.1: a) Light microscope image of a BP flake. The areas marked in green and red are approximately 5-7 layers thick. b) The same regions captured by the Ronchigram camera of the Nion UltraSTEM 100. c) Overview image captured by the HAADF detector shows the large amount of contamination present in the BP sample. Only the darker area in the middle is clean BP. d) FFT of the overview picture, (010), (110), (200) and (220) BP diffraction peaks are marked with green, white, red and yellow circles, respectively. The FFT shows clearly that we see BP in [001] (top-down) direction [89]. Scale bars are 20 µm (a), 10 µm (b), 2 nm (c) and 6 nm^{-1} (d)

of up to ca. 5.21 eV to the phosphorus atoms which is significantly closer to the displacement threshold energy for pristine BP. There are very few available values for displacement thresholds at defect sides and edges. For example Vierimaa et al. calculated threshold energies of 4.5 eV for adatom creation at Stones-Wales defects, a sputtering threshold of 4.5 eV for adatoms and an adatom creation threshold of 3.5 eV at single vacancy sites [71]. Das et al. calculated energy barriers of 5.13 eV for atom removal at AC edges and displacement thresholds between 5.57 eV and 6.23 eV for the different atoms at ZZ edges [91]. All of these values show that knock-on damage can play a role in the e-beam induced degradation of BP.

When Lee et al. did 80 kV TEM experiments with van der Waals stacks where a three-layer BP sample was shielded by graphene, they found severely reduced beam damage which they attribute to the graphene mitigating the radiolysis of BP through fast charge transfer. Sandwiching the BP between two graphene flakes reduced the e-beam damage even more, which made them conclude that radiolysis is the main damaging mechanism for bare BP samples [15]. Calculating cross-sections for knock-on damage and radiolytic processes of semi-conducting materials like BP is complicated because one has to consider excited states [72, 73], while measuring the cross-sections would require reasonably clean freestanding monolayer samples, which have not been produced until now [18, 20].

Also a third damage pathway has to be taken into consideration: Chemical etching through interaction with reactive species in the residual atmosphere of the STEM column, in the material itself or in the surface hydrocarbon contamination. The influence of the atmospheric composition on chemical etching of the contamination on graphene has been studied by Leuthner et al [92]. The contamination remained nearly unchanged under UHV conditions, while contamination surrounding clean areas of graphene was etched away when small amounts of O_2 or H_2O were introduced into the sample chamber, with the etching rate depending on the field of view of the scan. As we operated the Nion UltraSTEM 100 exclusively under vacuum levels below 10^{-10} mbar, the influence of the remaining atmosphere can be neglected. The second source for reactive species is the material itself. Although the setup was designed to avoid contamination in the fabrication and handling steps, there is no guarantee that the BP samples are completely free from oxygen. Most notably PDMS contains siloxanes which very likely introduce some oxygen into BP during the stamping process [11, 62]. The third source for reactive species is the hydrocarbon contamination typical for STEM samples [93]. Usually it is possible to remove most contamination by baking the samples in the loadlock for an extended period of time. However, this only works when dealing with adsorbed species which have relatively high vapour pressures at the baking

temperature, which is true for most weakly absorbed hydrocarbons [94]. In older STEM systems the major source of the contamination was oil vapour back-streaming from rotary or diffusion pumps. As modern microscopes are oil-free and operate under UHV conditions, the main source of the contamination is not the microscope but rather residuals on the sample holder, the TEM grid or the sample itself [93]. The extraordinary large amount of contamination on BP is often attributed to its high chemical reactivity and its puckered structure [19].

The importance of chemical etching as a damaging pathway of BP under the electron beam is emphasized by the observation that most damage appeared on the edge of the hydrocarbon contamination. Small defects appeared in the middle of a clean area but most of the times these defects heal or migrate out of the FOV already in the next frame. This observation lead to the hypothesis that most layers break apart due to chemical etching started by a reaction between the phosphorus atoms and reactive species (e.g. oxygen containing organic groups) in the hydrocarbon contamination. To check this hypothesis and to study the pristine BP surface in more detail we had to find the and suppress the source of the contamination or develop a reliable method to clean the BP samples in the vacuum system.

4.2 Sample cleaning

Several methods to clean exfoliated BP surfaces have been reported in literature. Lee et al. annealed their samples inside the TEM column at 270°C to remove contamination [18]. Das et al. annealed the samples at 250°C under a 90% Ar/ 10% H_2 atmosphere for 1 h [91]. Yao et al. annealed the sample in vacuum at 200°C in combination with an e-beam shower at a low dose rate of ca. 10^3 e^- $nm^{-2}s^{-1}$ for 5–10 min [19].

First we tried to anneal various samples at temperatures of 210°C, 230°C, 240°C and 270°C for 20 min on the heating plate inside the glovebox. No difference in regards to the contamination level could be seen. Then we tried to heat the SiN grid inside the UHV system using a pulsed 445 nm laser (spot diameter ca. 3 mm) with various power settings and illumination times. This method has been used to reliably clean graphene samples [86]. Illuminating the BP samples for 40 min with a laser power of 6.5 % of the maximum power (390 mW) did not improve the cleanliness at all, as can be seen in figure 4.4a. Illuminating the sample at 7 % laser power (420 mW) for 40 min did remove most of the thin phosphorene on the SiN grid. Remaining parts of the flake were riddled with holes and the covered area disintegrated rapidly under the electron beam after

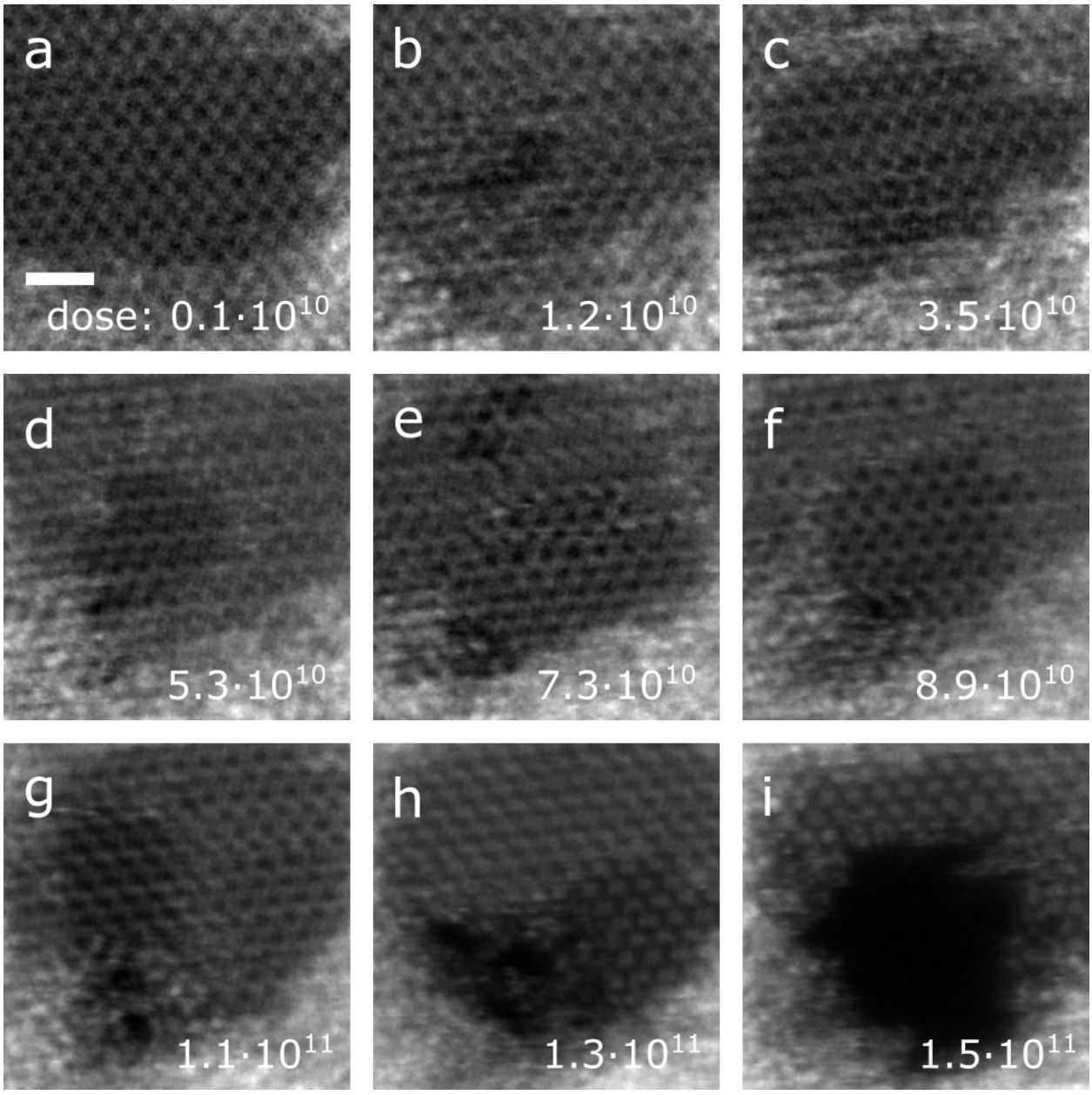

Figure 4.2: The thinning of a reasonably clean area of BP under electron irradiation imaged by HAADF. The images contain the accumulated electron dose until the respective image. Scale bar 2 nm (all images).

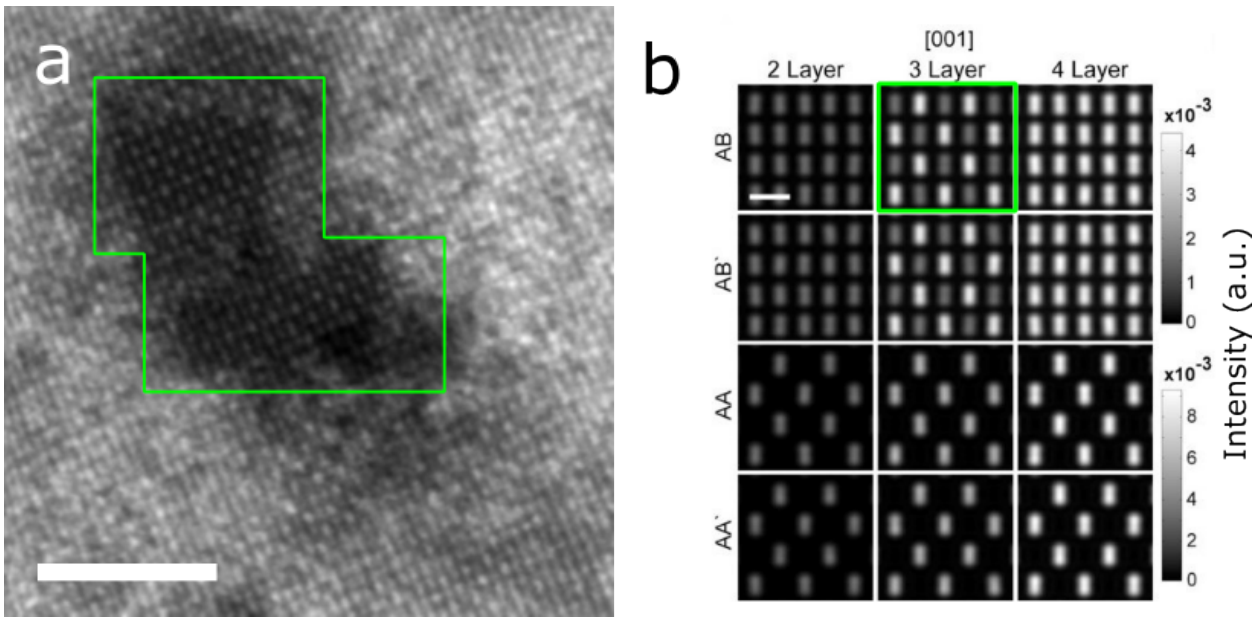

Figure 4.3: a) MAADF image of a clean sample area with AB (or AB') stacking order (green area) that can be attributed to three-layered BP. b) Simulated MAADF images of black-phosphorus with AB, AB', AA' and AA stacking order in [001] and [101] crystallographic direction. Reprinted with permission from [11]. Copyright 2015, American Vacuum Society. Scale bars 5 nm (a) and 4 Å (b).

increasing the magnification (see figures 4.4b and 4.4c). Higher laser powers introduced damage into the SiN grid itself or even ripped the grid apart.

Next we tried to heat the sample using the 473 nm pulsed laser in the STEM column with a spot size of of ca. 40×45 µm^2 The individual holes on the used SiN grid window have a diameter of 2 µm, are arranged in a single 50×50 matrix and separated by 5 µm, thus directing the laser to a specific hole in a window will not only affect one hole, but large parts of the window. We centered the laser to a thin-layer flake which partially covered a hole. Beginning with a 10 ms and 5 mW pulse, we increased the laser power subsequently until we saw the first effect when we illuminated the sample with 40 mW for 100 ms. After the first pulse with these parameters the area towards the uncovered hole lost a lot of contrast, which we first interpreted as a cleaning effect. A second pulse with these parameters didn't affect the mentioned area but did reduce the contrast on the rest of the flake. After a third and a fourth 40 mW pulse (150 ms and 200 ms, respectively) we recorded an overview image and saw increased contamination at formerly scanned areas in comparison to unscanned areas. Also no FFT spots were visible in the FFT of the image, which could be an indicator for the amorphization of the material. To check whether this was caused by the local laser illumination, or if the whole sample was destroyed, we imaged a thicker area,

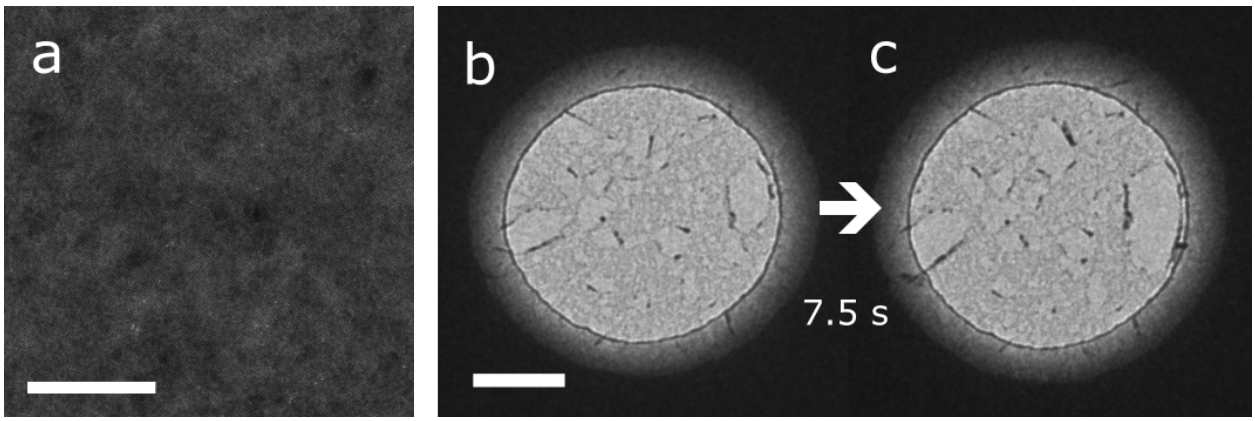

Figure 4.4: The results of cleaning experiments using the 445 nm in the target-chamber. a) Illumination with 390 mW for 40 min showed no cleaning effect at all. b-c) Illumination with 420 mW for 40 min damaged the structure severely. After about 7.5 seconds under the electron beam the holes have grown significantly. Scale bars 5nm (a) and scale bar 1 µm (b-c).

where we could clearly see FFT spots associated with crystalline BP [18]. Then we returned to the seemingly amorphized flake and illuminated it repeatedly with increasing laser power and illumination time. After 15 pulses with increasing laser power, the last of which had a power of 56 mW for 100 ms, most parts of the flake had a uniform contrast, but still no FFT spots were visible. The flake still exhibited sharp edges and a few spots with high contrast appeared near to the edge to the uncovered hole, which we interpreted as clusters. When we imaged the edges of the SiN grid we could clearly see blisters in the SiN. To avoid further damage in the SiN grid we moved to another, thicker area and illuminated it with a 39 mW and 1 ms pulse. In contrast to the flake before, the thicker flake became riddled with holes and disintegrated immediately under the electron beam when we increased the magnification. Another thicker area was targeted with a 37 mW and 1 ms pulse. Also in this case the flake became riddled with holes and disintegrated under the electron beam once we tried to image it with a high magnification (see figure 4.5). The difference in reaction to the illumination between flakes of different thickness could be attributed to the relation between the bandgap and the layer number but additional data would be needed to confirm this hypothesis.

To confirm the amorphous nature of the illuminated thin-layered sample we obtained CBED images. Figure 4.6 shows CBED images at three different locations. Focusing the beam on the uncovered area showed no diffraction spots as expected. When the beam is directed to a cluster on the edge to the uncovered area a clear diffraction structure with diffraction spots and a clear ring pattern typical for poly-crystalline materials could be observed. Th clusters probably contain large amounts of phosphorus atoms or heavier elements, as indicated by the higher contrast. The

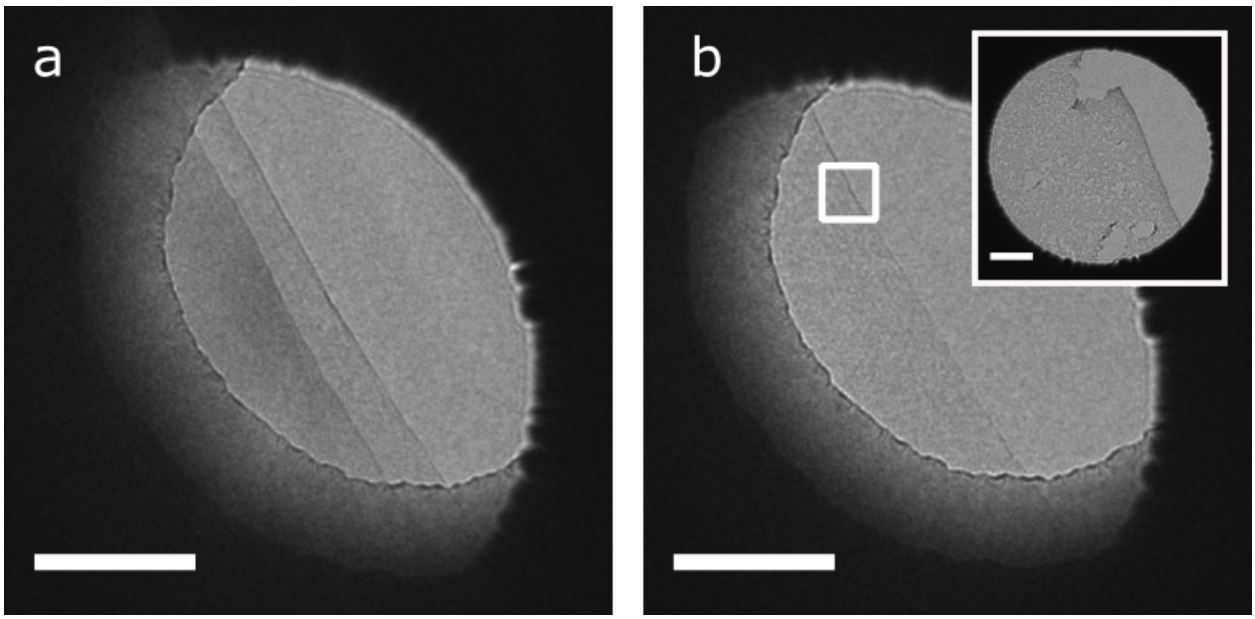

Figure 4.5: The results of cleaning experiments using the 473 nm laser inside the STEM column in the Ronchigram camera . a) A thicker BP flake before illumination b) After illumination with a 39 mW 1 ms pulse the flake is considerably thinner and shows lots of damage. Inset: The squared area in higher magnification, the remnants of the BP rip apart under the electron beam. Scale bars 400 nm (a,b) and 40 nm (inset).

CBED image of the flake shows no diffraction spots and a very washed out ring-like structure. This pattern is typical for amorphous materials [68] and confirms our hypothesis that the illumination transformed the crystalline BP structure into a (remarkably stable) amorphous structure.

After the laser heating experiments turned out to be unsuccessful, we tried to "etch" away the contamination by annealing the sample inside the loadlock at temperatures of up to 180°C under a varigon atmosphere (5% hydrogen, 95% argon). We flushed the loadlock once with varigon to remove oxygen residuals before introducing the samples into the loadlock using the connection to the glovebox. When the connecting valve was opened, the oxygen detectors in the glovebox observed an oxygen amount of up to 100 ppm which quickly dropped below 20 ppm after 2 min. This leakage could be attributed to an incompatible gas blocker which was inserted to block the argon inlet of the loadlock. Inspection in the STEM showed less contrast in the contaminated areas in comparison to uncleaned samples which could be attributed to thinner contamination but no clear indication for cleaning could be found.

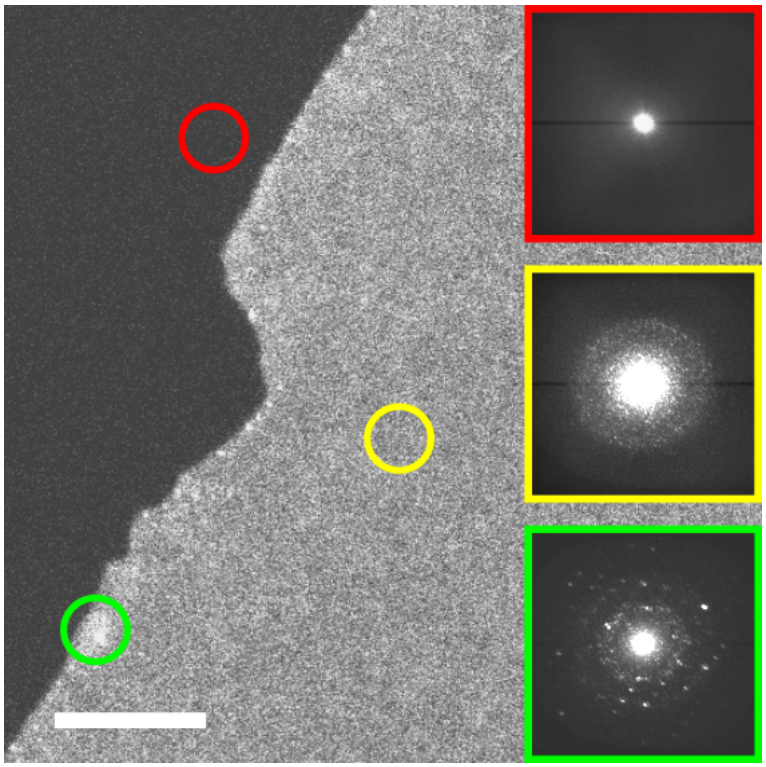

Figure 4.6: HAADF image with CBED images at three different positions of the lasered flake, imaged by the Ronchigram camera. Red: CBED of the vacuum region. Yellow: CBED of the lasered phosphorene flake. Green: CBED of a cluster on the edge of the flake. Scale bar: 200 nm.

4.3 BP-graphene heterostructures

BP/G heterostructures were prepared as described in section 3.2.3 to replicate the studies by Lee et al [17, 18]. The advantage of layering BP on a sheet of graphene is an increased stability under the electron beam as the graphene layer reduces radiolytic damage in the phosphorene through fast charge transport [17]. The samples were inserted into the STEM such that the e-beam hits the BP first (thus they are named BP/G samples). The orientation of the heterostructure may play a role in the damaging mechanism, but Lee at al. reported no significant difference between the two configurations [17]. There are a few differences between Lee et al. and our study: First, our BP samples are handled exclusively inside the CANVAS system, while Lee et al. produced their samples inside a nitrogen-filled glovebox but exposed them to ambient conditions for an undisclosed amount of time during the transfer to the TEM. Secondly, we prepared the monolayer graphene substrate by wet transfer of Graphenea© Easy transfer graphene, whereas Lee et al. exfoliated graphene samples of undisclosed thickness with the scotch-tape method [4] and transferred them using the PDMS transfer method. Additionally, we imaged our samples with a 60 kV STEM at a pressure of ca. 10^{-10} mbar, while Lee et al. imaged their samples with a 80 kV TEM at a pressure of ca. $1 \cdot 10^{-7}$ mbar.

Figure 4.7a shows a Ronchigram image of a BP/G heterostructure. A few distinct features are clearly visible: The region marked with G is partially clean monolayer graphene as can be seen in a higher magnification MAADF picture (figure 4.7b). This region contains stripe-like higher contrast features that can be identified with hydrocarbon contamination similar to the one observed by Pálinkás et al [61]. The observation of these contamination stripes is not surprising as the graphene samples were stored for at least 12 h under ambient conditions before being introduced into the argon atmosphere. Note that this kind of contamination on graphene samples is usually highly volatile and its micro-structure can only be observed with sensitive methods like PeakForce tapping AFM[1] [61]. Annealing inside the glovebox may have helped removing some of the contamination but large clean areas of graphene can only be produced by in-situ annealing [85] or laser cleaning under UHV condition [86].

The region marked with BP/G is the actual vdW heterostructure with BP of varying thickness stacked on the graphene monolayer. The high contrast areas within the BP/G are dirt pockets,

[1] In PeakForce tapping AFM, the tip periodically taps the sample and the interaction force (typically only pN) is measured directly by the deflection of the cantilever. The low imaging forces allow the resolution of atomic scale structures without destroying the samples integrity.

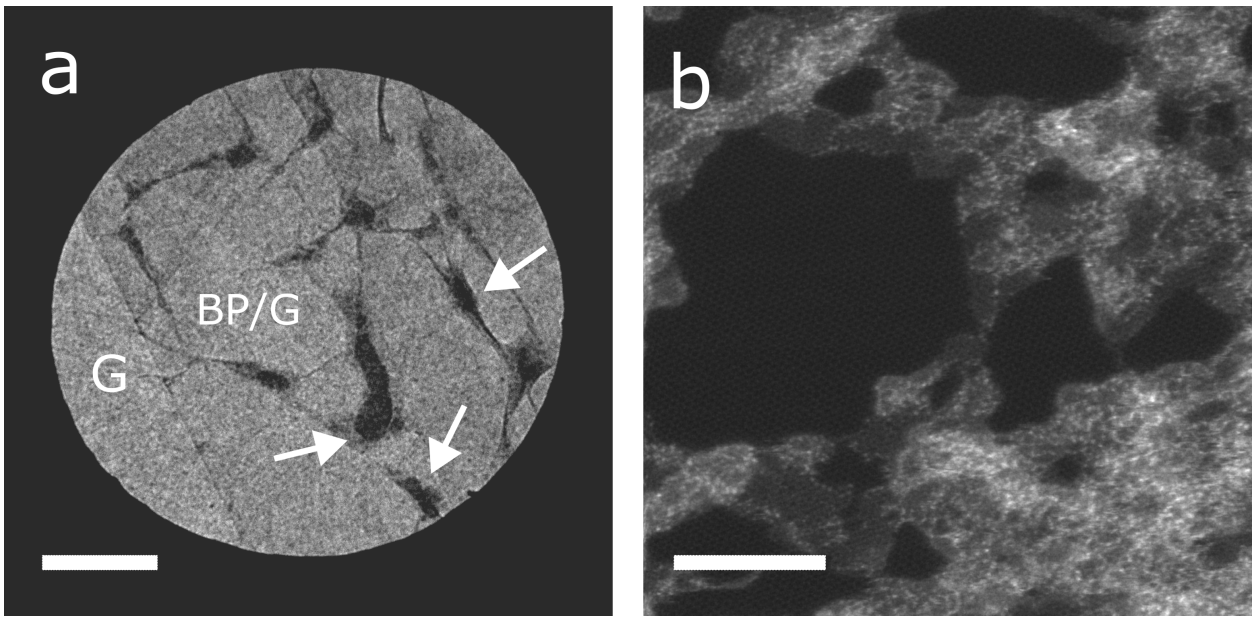

Figure 4.7: a) Ronchigram overview picture of a BP/G heterostructure with uncovered graphene (left side) and BP/G heterostructure (right). The dark areas within the BP/G (some of them marked by white arrows) consist of contamination trapped between the layers [62] b) MAADF image of the bare monolayer graphene with large contamination islands. Scale bars 0.5 µm (a) and 4 nm (b).

typical for vdW heterostructures as described in section 2.3. The BP part of the vdW stack is heavily covered with contamination, very similar to what was observed for bare BP. After finding a somewhat clean area with a size of ca. 2 nm^2, the area was imaged with HAADF for 45 min. In figure 4.8a the area before the measurement is shown. After about 10 min the first layer began to disintegrate (image 4.8b). This layer, which can easily be identified as an uneven amount of layers (very likely trilayer) by looking at the stacking order, disintegrated after about 23 min of irradiation (image 4.8c). The uncovered bilayer seemed to be less stable as the first pores appeared after about 26 min (image 4.8d). After 34 min remnants of a monolayer (note that in the [001] direction a monolayer looks identical to an AA-stacked bilayer as can be seen in the model of Wu et al. 4.3b) were visible for a few frames until the underlying graphene substrate was uncovered (image 4.8e). Image 4.8f shows the irradiated area after about 39 min. The uncovered graphene area is surrounded by few-layered BP, small parts of this area could be attributed to a trilayer, the rest is probably a bilayer. Once the pore reached contaminated areas it did not grow significantly over the observed timeframe. In contrast to the observations made by Lee et al., no large areas of stable BP monolayers could be imaged. This may be related to the higher electron dose per time unit and area at this magnification in the STEM compared to the TEM used by Lee et al., but may also be associated to the large amount of contamination present in

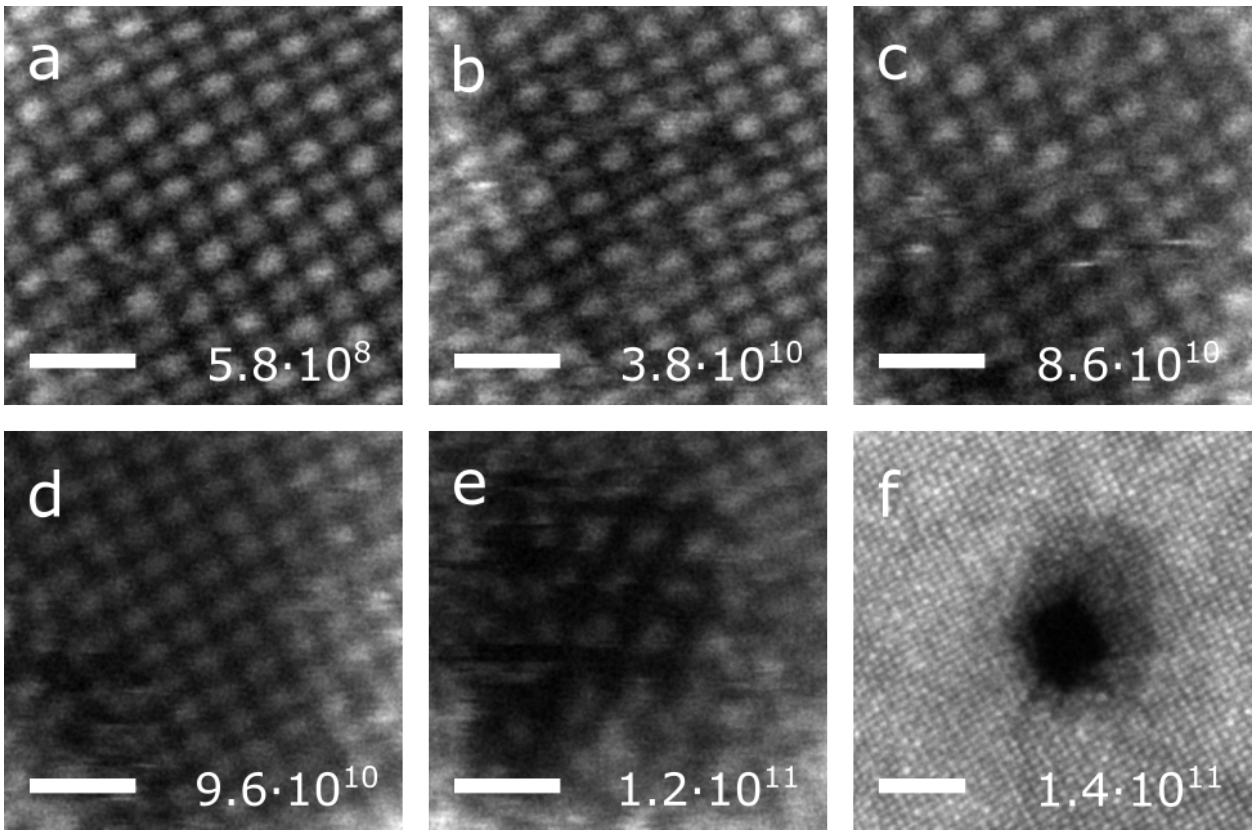

Figure 4.8: HAADF images of the thinning of a BP/G heterostructure under the electron beam. The images contain the accumulated electron dose until the respective image. Inset: By adjusting the contrast and brightness settings the graphene lattice becomes visible. Scale bars 1 nm (a-e, inset) and 10 nm (f).

our samples. The presence of graphene below the BP layer can be confirmed by adjusting the contrast settings to make the hexagonal pattern of graphene visible in the HAADF (see inset in 4.8f).

Even after prolonged irradiation (up to 1 h) the uncovered graphene lattice showed no structural damage. The structural strength of graphene under the electron beam can be explained by its metallic nature, which prevents damage by electrolysis, and by the practically non-existent knock-on damage cross section at 60 kV irradiation [95]. Using the moving lattice model from 4.1 with a Debye temperature of $\Theta_D = 1287$ K from literature [95] we calculate that a significant amount of 60 keV electrons can transfer energies up to 13 eV to the carbon atoms, well below the displacement threshold in graphene of 22 eV [96]. Chemical etching can lead to damage only at preexisting defect sites [92], so in conclusion the pristine graphene layer should remain unaffected by the 60 kV electron beam.

4.4 EELS measurements

To get further insights into the oxidation state of our samples, we performed EELS measurements. First we obtained EELS point spectra at different positions of the varigon-cleaned BP/G sample. We used this sample for the first measurement, because it looked cleaner than the other samples. Figure 4.9a-c shows background subtracted spectra of the oxygen K edge at a dirt pocket, at a contamination cluster, and at the slightly contaminated sample surface. Whereas at the probe position 4.9c the oxygen signal is barely visible, the EELS spectrum on the contamination cluster shows clearly two features centered at ca. 532 eV and ca. 540 eV, respectively. The spectrum at the dirt pocket shows only one feature at 540 eV. Additionally we obtained point spectra of the phosphorus L edge, which looked very similar at every probe position. Figure 4.9d shows one of the phosphorus L edge spectra with a sharp peak-like feature at ca. 131.5 eV, an intermediate peak at ca. 138 eV, a long ridge-like feature with peak around 155 eV and an additional peak at ca. 188 eV.

Comparing our spectra to the data from a similar EELS study [89] it becomes evident that the sample has undergone some oxidation. The phosphorus L edge of clean phosphorene starts at around 132 eV and has a peak at ca. 188 eV, whereas the phosphorus L edge of phosphorus oxides P_xO_y begins at ca. 137.5 at has a peak around 193 eV [89]. The observation of the structure associated with P_xO_y makes it clear that at least parts of the sample have undergone oxidation [10, 12]. Phosphorus L edge spectra obtained at dirt pockets and contamination clusters had the same overall structure but smaller signal-to-noise ratio. This may lead to the interpretation that the sample surface is more or less uniformly oxidized and the oxidation state does not depend on the local contamination density. The other clear indicator for oxidation is the presence and structure of the oxygen K edge as it looks very similar to spectra of samples exposed to ambient conditions for two days [89]. The amplitude of the oxygen peak seems to correlate with the local contamination thickness, which suggests that most oxygen atoms are introduced via the contamination and are not intrinsic to the material. We were not able to attribute the absence of the oxygen feature at ca. 532 eV at dirt pockets to any physical origin, mostly due to the lack of comparable data.

As the small leak during the varigon cleaning experiment, the storage time inside the glovebox or the varigon cleaning procedure itself may have contributed to the significant oxidation, we repeated the measurements with a BP sample that was introduced into the UHV system about 30 min after exfoliation. Figure 4.10a shows a low-resolution HAADF image of this sample.

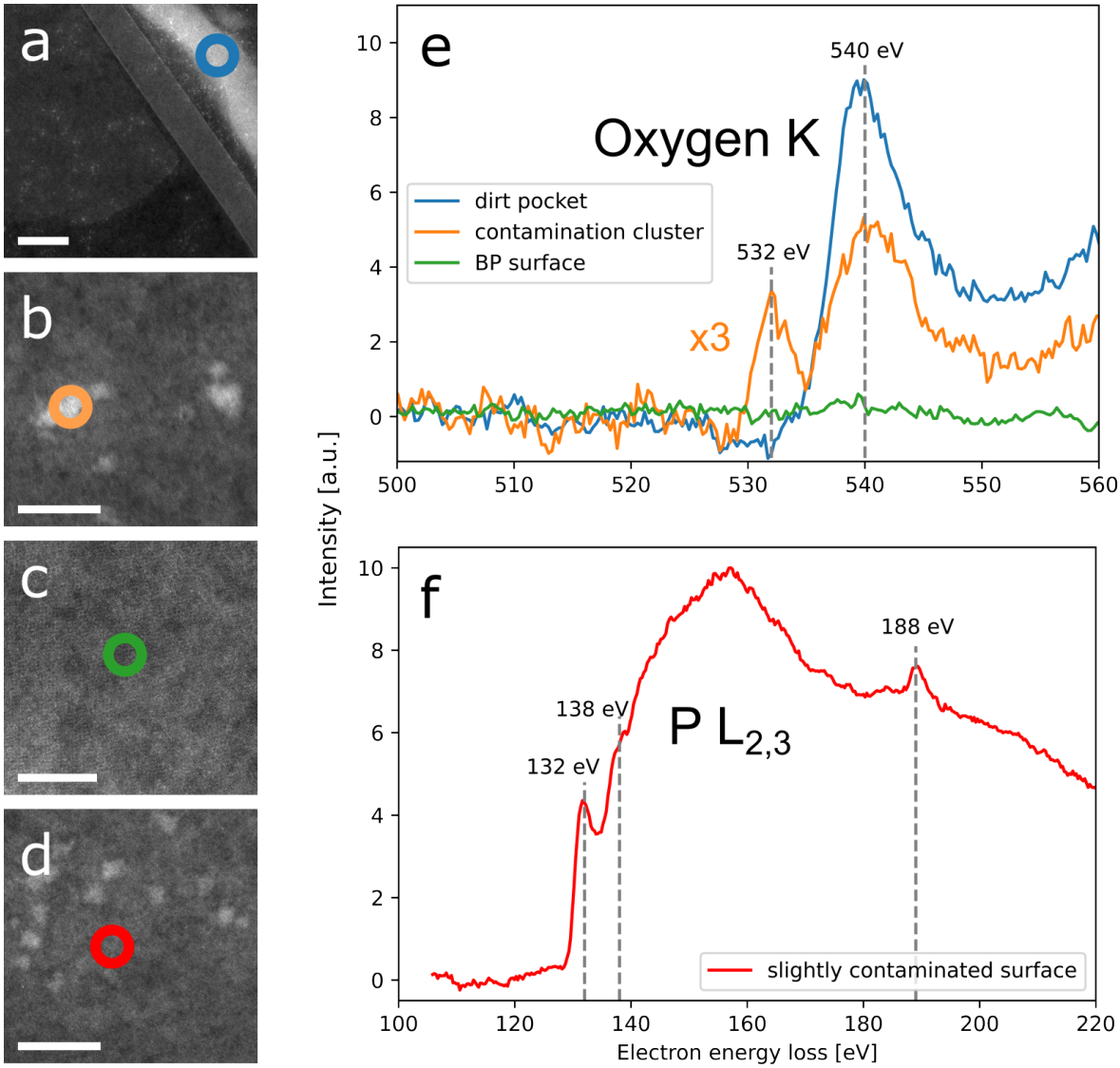

Figure 4.9: EELS point spectra at different locations of the sample. a-d) HAADF images showing the position of the beam during EELS acquisition at a "dirt pocket" (blue), at a contamination cluster (orange) and at two spots on the contaminated sample surface (green and red). e) EEL spectra of the oxygen K-edge at the color-coded positions a-c. f) EEL spectrum of the phosphorus L edge at the position d. Scale bars 50 nm (a), 10 nm (b,d) and 5 nm (c).

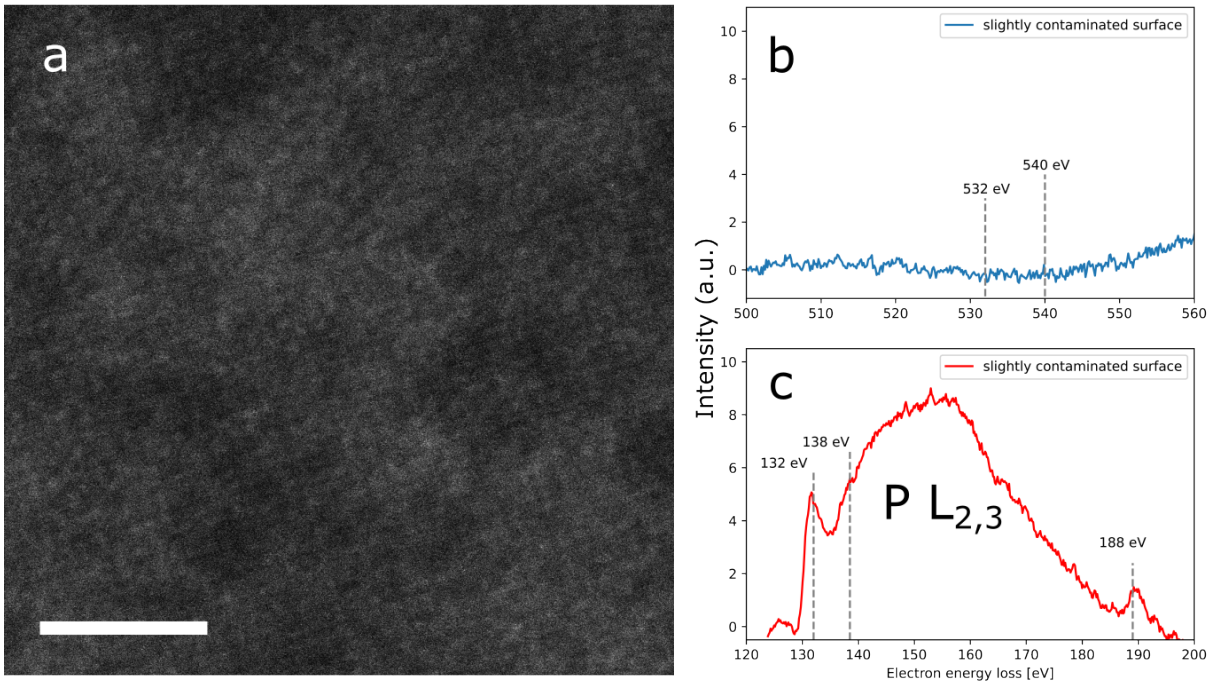

Figure 4.10: Sample introduced into UHV system after transfer. a) HAADF image of the sample without contamination clusters. b) EEL spectrum at the oxygen K-edge region. c) EEL spectrum of the phosphorus L edge. Scale bar 2 nm

The sample was particularly less contaminated than samples that were stored inside the glovebox for at least several hours. Most notably, no contamination clusters could be observed. EELS measurements of the slightly contaminated surface (figure 4.10b-c) showed no oxygen K edge, but a phosphorus L edge which had the fine structure at ca. 238 eV. A possible interpretation is that the BP surface had some contact with oxygen, but the amount of oxygen present in the thin contamination is not enough to produce a measurable oxygen K edge.

To conclude: Firstly, storage inside the glovebox is not ideal for BP samples because they accumulate hydrocarbon contamination from the environment over time. Secondly, even a short exposure to a small partial pressure of oxygen may lead to measurable changes in BP chemistry. Thirdly, it is very likely that the contamination is the major source for oxygen atoms, as indicated by the strong oxygen K-edge at heavily contaminated areas.

Chapter 5

Conclusion and outlook

The primary goal of this study was the fabrication of few-layer BP samples inside the CANVAS system. After switching from PPC to the PDMS transfer method, this was accomplished. The transfer turned out to be reliable, reproducible and the technique can easily be learned within a few hours. It should be noted that the exfoliation of a monolayer BP flake using the PDMS method seems to be impossible. The thinnest flakes we could fabricate had 3-4 layers. Other groups were able to produce samples of similar thickness but to our knowledge the exfoliation of a monolayer has never been reported.

Although we were successful in obtaining atomic resolution images of few layered BP, quantitative measurements were severely hindered by the large amount of contamination encountered on the samples surfaces. Various sample cleaning methods were tested. Illuminating the sample with the 445 nm laser inside the "target-chamber" did not lead to useful results. Illumination with the 473 nm laser in the STEM column did transform a thin BP sample into an amorphous phosphorus species, which is remarkably stable to further laser treatment. Unfortunately this could not be reproduced by illuminating other (although thicker) flakes. Additionally, baking samples inside a H_2/Ar atmosphere was tested which also did not clean the samples, although it could be successful if it would be possible to elevate loadlock temperatures from 180°C to over 270°C. The most promising cleaning method seems to be in-situ annealing. To implement this method an UHV annealing device has been designed and ordered. Unfortunately, the device has not been installed at the time of writing this thesis due to delayed delivery of crucial parts. An even more promising approach is the installation of an annealing device directly in the STEM column. At the time of writing this thesis one such device, the "electrical puck" is already in trial use. In order to use this device, BP has to be transferred onto specialized Protochips© TEM grids which

so far has not been tested.

We observed layer-by-layer thinning of BP under the electron beam. The discussion of the e-beam induced damage let to no clear evidence of a preferred damage pathway. Most probably all three pathways, knock-on damage, electrolysis and chemical etching play some role in BP damage under the electron beam. However we note that the role of the contamination in the damage process should not be underestimated, as the fact that most major defects appear next to contaminated areas is a strong indicator for chemical etching due to reactive species in the contamination. The presence of oxygen inside the contamination was confirmed by STEM-EELS. Before the degradation of BP under the electron beam could be studied systematically, reasonably clean samples have to be fabricated to exclude the contamination as a limiting parameter.

BP/G heterostructures have been fabricated successfully. These heterostructures show indeed higher stability under the e-beam which could be explained by lower electrolytic damage due to fast charge transfer from the graphene layer. In contrast to very similar experiments in literature, monolayer BP could not be observed for a reasonable amount of time, which is most probably related to the large amount of contamination.

Given reasonably clean samples, BP/G samples could be studied in a similar way Åhlgren et al. [97] studied the degradation of MoS_2 and $MoTe_2$. After thinning down the samples to monolayer thickness, the growth rate of BP pores could be measured as a function of oxygen partial pressure to get further insight into the degradation mechanisms. Once the production of clean large area single-layered BP becomes possible, more elaborate experiments like the measurement of interaction cross sections could be done.

An important consideration for future experiments is the amount of oxygen the BP has already encountered before entering the STEM column. Some amount of pre-oxidation seems to be unavoidable due to several reasons: Firstly, some oxygen from the (partially) oxidized bulk BP may translate to the cleaved flakes. Secondly, some oxygen may be introduced by the PDMS stamp. Thirdly, the hydrocarbon contamination may introduce oxygen into the BP before cleaning. In that sense annealing the sample to remove contamination may even be counterproductive as the thermal energy may facilitate the oxidation.

To eliminate the PDMS as a contamination source, polymer-free transfer techniques could be implemented. One potential technique would be the direct pick-up of BP from a substrate to a modified SiN grid, similar to the method described by Wendong Wang [98].

This thesis provides the groundwork for the future production of high quality, oxidation-free phosphorene samples. Once the presented hurdles are overcome, the advantages of working within the CANVAS system will be shown in full power.

Bibliography

[1] Wallace, P. R. The band theory of graphite. *Physical Review* **71**, 622–634 (1947). DOI: 10.1103/PhysRev.71.622.

[2] Peierls, R. Bemerkungen über umwandlungstemperaturen. *Helvetica physica acta* **7**, 81 (1934). DOI: 10.5169/seals-110415.

[3] Landau, L. D. On the theory of phase transitions. ii. *Phys. Z. Sowjet.* **11**, 545 (1937). DOI: 10.1038/138840a0.

[4] Novoselov, K. S. *et al.* Electric field effect in atomically thin carbon films. *Science* **306**, 666–669 (2004). DOI: 10.1126/science.1102896.

[5] Geim, A. K. & Novoselov, K. S. The rise of graphene. *Nature Materials* **6**, 183–191 (2007). DOI: 10.1038/nmat1849.

[6] Novoselov, K. S. *et al.* Two-dimensional atomic crystals. *Proceedings of the National Academy of Sciences* **102**, 10451–10453 (2005). DOI: 10.1073/pnas.0502848102.

[7] Koenig, S. P., Doganov, R. A., Schmidt, H., Neto, A. H. C. & Özyilmaz, B. Electric field effect in ultrathin black phosphorus. *Applied Physics Letters* **104** (2014). DOI: 10.1063/1.4868132.

[8] Carvalho, A. *et al.* Phosphorene: from theory to applications. *Nature Reviews Materials* **1**, 16061 (2016). DOI: 10.1038/natrevmats.2016.61.

[9] Holler, J. *et al.* Air tightness of hbn encapsulation and its impact on raman spectroscopy of van der waals materials. *2D Materials* **7**, 015012 (2020). DOI: 10.1088/2053-1583/ab4723.

[10] Huang, Y. *et al.* Interaction of black phosphorus with oxygen and water. *Chemistry of Materials* **28**, 8330–8339 (2016). DOI: 10.1021/acs.chemmater.6b03592.

[11] Wu, R. J. *et al.* Atomic and electronic structure of exfoliated black phosphorus. *Journal of Vacuum Science and Technology A: Vacuum, Surfaces, and Films* **33**, 060604 (2015). DOI: 10.1116/1.4926753.

[12] Favron, A. *et al.* Photooxidation and quantum confinement effects in exfoliated black phosphorus. *Nature Materials* **14**, 826–832 (2015). DOI: 10.1038/nmat4299.

[13] Kuntz, K. L. *et al.* Control of surface and edge oxidation on phosphorene. *ACS Applied Materials and Interfaces* **9**, 9126–9135 (2017). DOI: 10.1021/acsami.6b16111.

[14] Naclerio, A. E. *et al.* Visualizing oxidation mechanisms in few-layered black phosphorus via in situ transmission electron microscopy. *ACS Applied Materials and Interfaces* **12**, 15844–15854 (2020). DOI: 10.1021/acsami.9b21116.

[15] Lee, Y. *et al.* Atomic-scale imaging of few-layer black phosphorus and its reconstructed edge. *Journal of Physics D: Applied Physics* **50** (2017). DOI: 10.1088/1361-6463/aa5583.

[16] Laurent, B. S., Dey, D., Yu, L. & Hollen, S. Atomic-scale investigation of oxidation at the black phosphorus surface. *ACS Applied Electronic Materials* **3**, 4066–4072 (2021). DOI: 10.1021/acsaelm.1c00558.

[17] Lee, Y. *et al.* Fabrication and imaging of monolayer phosphorene with preferred edge configurations via graphene-assisted layer-by-layer thinning. *Nano Letters* **20**, 559–566 (2020). DOI: 10.1021/acs.nanolett.9b04292.

[18] Lee, S. *et al.* Atomically sharp, closed bilayer phosphorene edges by self-passivation. *ACS Nano* **16**, 12822–12830 (2022). DOI: 10.1021/acsnano.2c05014.

[19] Yao, F. *et al.* In situ transmission electron microscopy study of the formation and migration of vacancy defects in atomically thin black phosphorus. *2D Materials* **8** (2021). DOI: 10.1088/2053-1583/abce09.

[20] Baboukani, A. R. *et al.* Defects investigation of bipolar exfoliated phosphorene nanosheets. *Surface Science* **720**, 122052 (2022). DOI: 10.1016/j.susc.2022.122052.

[21] Mangler, C. *et al.* A materials scientist's canvas: A system for controlled alteration of nanomaterials in vacuum down to the atomic scale. *Microscopy and Microanalysis* **28**, 2940–2942 (2022). DOI: 10.1017/s1431927622011023.

[22] Bridgman, P. W. Two new modifications of phosphorus. *Journal of the American Chemical Society* **36**, 1344–1363 (1914). DOI: 10.1021/ja02184a002.

[23] Liu, H. *et al.* Phosphorene: An unexplored 2d semiconductor with a high hole mobility. *ACS Nano* **8**, 4033–4041 (2014). DOI: 10.1021/nn501226z.

[24] Molas, M. R. *et al.* Photoluminescence as a probe of phosphorene properties. *npj 2D Materials and Applications* **5** (2021). DOI: 10.1038/s41699-021-00263-8.

[25] Xia, F., Wang, H. & Jia, Y. Rediscovering black phosphorus as an anisotropic layered material for optoelectronics and electronics. *Nature Communications* **5**, 4458 (2014). DOI: 10.1038/ncomms5458.

[26] Jiang, J. W. & Park, H. S. Negative poisson's ratio in single-layer black phosphorus. *Nature Communications* **5**, 4727 (2014). DOI: 10.1038/ncomms5727.

[27] Tran, V., Soklaski, R., Liang, Y. & Yang, L. Layer-controlled band gap and anisotropic excitons in few-layer black phosphorus. *Physical Review B* **89**, 235319 (2014). DOI: 10.1103/PhysRevB.89.235319.

[28] Miao, J., Zhang, L. & Wang, C. Black phosphorus electronic and optoelectronic devices. *2D Materials* **6**, 032003 (2019). DOI: 10.1088/2053-1583/ab1ebd.

[29] Li, B. *et al.* Black phosphorus, a rising star 2d nanomaterial in the post-graphene era: Synthesis, properties, modifications, and photocatalysis applications. *Small* **15**, 1804565 (2019). DOI: 10.1002/smll.201804565.

[30] Duan, S. *et al.* Enhanced thermoelectric performance in black phosphorene via tunable interlayer twist. *Small* **18**, 2204197 (2022). DOI: 10.1002/smll.202204197.

[31] Naqvi, B. A. *et al.* Visualizing degradation of black phosphorus using liquid crystals. *Scientific Reports* **8**, 12966 (2018). DOI: 10.1038/s41598-018-31067-4.

[32] Li, W. *et al.* Phosphorene degradation: Visualization and quantification of nanoscale phase evolution by scanning transmission x-ray microscopy. *Chemistry of Materials* **32**, 1272–1280 (2020). DOI: 10.1021/acs.chemmater.9b04811.

[33] Nan, H. *et al.* Effect of the surface oxide layer on the stability of black phosphorus. *Applied Surface Science* **537**, 147850 (2021). DOI: 10.1016/j.apsusc.2020.147850.

[34] Zhou, Q., Chen, Q., Tong, Y. & Wang, J. Light-induced ambient degradation of few-layer black phosphorus: Mechanism and protection. *Angewandte Chemie* **128**, 11609–11613 (2016). DOI: 10.1002/ange.201605168.

[35] Pei, J. *et al.* Producing air-stable monolayers of phosphorene and their defect engineering. *Nature Communications* **7**, 10450 (2016). DOI: 10.1038/ncomms10450.

[36] Ziletti, A., Carvalho, A., Campbell, D. K., Coker, D. F. & Neto, A. H. C. Oxygen defects in phosphorene. *Physical Review Letters* **114**, 046801 (2015). DOI: 10.1103/PhysRevLett.114.046801.

[37] Utt, K. L. *et al.* Intrinsic defects, fluctuations of the local shape, and the photo-oxidation of black phosphorus. *ACS Central Science* **1**, 320–327 (2015). DOI: 10.1021/acscentsci.5b00244.

[38] Hyun, C., Kim, J. H., Lee, J. Y., Lee, G. H. & Kim, K. S. Atomic scale study of black phosphorus degradation. *RSC Advances* **10**, 350–355 (2019). DOI: 10.1039/c9ra08029e.

[39] Yang, G., Li, L., Lee, W. B. & Ng, M. C. Structure of graphene and its disorders: a review. *Science and Technology of Advanced Materials* **19**, 613–648 (2018). DOI: 10.1080/14686996.2018.1494493.

[40] Chen, Z., Gandhi, U., Lee, J. & Wagoner, R. Variation and consistency of young's modulus in steel. *Journal of Materials Processing Technology* **227**, 227–243 (2016). DOI: 10.1016/j.jmatprotec.2015.08.024.

[41] Neto, A. H. C., Guinea, F., Peres, N. M. R., Novoselov, K. S. & Geim, A. K. The electronic properties of graphene. *Reviews of Modern Physics* **81**, 109–162 (2009). DOI: 10.1103/RevModPhys.81.109.

[42] Meyer, J. C. *et al.* The structure of suspended graphene sheets. *Nature* **446**, 60–63 (2007). DOI: 10.1038/nature05545.

[43] Bolotin, K. *et al.* Ultrahigh electron mobility in suspended graphene. *Solid State Communications* **146**, 351–355 (2008). DOI: 10.1016/j.ssc.2008.02.024.

[44] Balandin, A. A. *et al.* Superior thermal conductivity of single-layer graphene. *Nano Letters* **8**, 902–907 (2008). DOI: 10.1021/nl0731872.

[45] Mayorov, A. S. *et al.* Micrometer-scale ballistic transport in encapsulated graphene at room temperature. *Nano Letters* **11**, 2396–2399 (2011). DOI: 10.1021/nl200758b.

[46] Blake, P. *et al.* Making graphene visible. *Applied Physics Letters* **91**, 063124 (2007). DOI: 10.1063/1.2768624.

[47] Geim, A. K. & Grigorieva, I. V. Van der waals heterostructures. *Nature* **499**, 419–425 (2013). DOI: 10.1038/nature12385.

[48] Dean, C. R. *et al.* Boron nitride substrates for high-quality graphene electronics. *Nature Nanotechnology* **5**, 722–726 (2010). DOI: 10.1038/nnano.2010.172.

[49] Doganov, R. A. *et al.* Transport properties of ultrathin black phosphorus on hexagonal boron nitride. *Applied Physics Letters* **106**, 083505 (2015). DOI: 10.1063/1.4913419.

[50] Bellus, M. Z., Ceballos, F., Chiu, H.-Y. & Zhao, H. Tightly bound trions in transition metal dichalcogenide heterostructures. *ACS Nano* **9**, 6459–6464 (2015). DOI: 10.1021/acsnano.5b02144.

[51] Liang, S. J., Cheng, B., Cui, X. & Miao, F. Van der waals heterostructures for high-performance device applications: Challenges and opportunities. *Advanced Materials* **32**, 1903800 (2020). DOI: 10.1002/adma.201903800.

[52] Nourbakhsh, A., Zubair, A., Dresselhaus, M. S. & Palacios, T. Transport properties of a mos 2/wse2 heterojunction transistor and its potential for application. *Nano Letters* **16**, 1359–1366 (2016). DOI: 10.1021/acs.nanolett.5b04791.

[53] Liao, W., Huang, Y., Wang, H. & Zhang, H. Van der waals heterostructures for optoelectronics: Progress and prospects. *Applied Materials Today* **16**, 435–455 (2019). DOI: 10.1016/j.apmt.2019.07.004.

[54] Li, H. *et al.* Constructing van der waals heterostructures by dry-transfer assembly for novel optoelectronic device. *Nanotechnology* **33**, 465601 (2022). DOI: 10.1088/1361-6528/ac5f96.

[55] Liu, Z. *et al.* Direct growth of graphene/hexagonal boron nitride stacked layers. *Nano Letters* **11**, 2032–2037 (2011). DOI: 10.1021/nl200464j.

[56] Gong, Y. *et al.* Vertical and in-plane heterostructures from ws2/mos2 monolayers. *Nature Materials* **13**, 1135–1142 (2014). DOI: 10.1038/nmat4091.

[57] Yankowitz, M. *et al.* Emergence of superlattice dirac points in graphene on hexagonal boron nitride. *Nature Physics* **8**, 382–386 (2012). DOI: 10.1038/nphys2272.

[58] Woods, C. R. *et al.* Commensurate–incommensurate transition in graphene on hexagonal boron nitride. *Nature Physics* **10**, 451–456 (2014). DOI: 10.1038/nphys2954.

[59] Haigh, S. J. *et al.* Cross-sectional imaging of individual layers and buried interfaces of graphene-based heterostructures and superlattices. *Nature Materials* **11**, 764–767 (2012). DOI: 10.1038/nmat3386.

[60] Argentero, G. *et al.* Unraveling the 3d atomic structure of a suspended graphene/hbn van der waals heterostructure. *Nano Letters* **17**, 1409–1416 (2017). DOI: 10.1021/acs.nanolett.6b04360.

[61] Pálinkás, A. *et al.* The composition and structure of the ubiquitous hydrocarbon contamination on van der waals materials. *Nature Communications* **13**, 6770 (2022). DOI: 10.1038/s41467-022-34641-7.

[62] Schwartz, J. J. *et al.* Chemical identification of interlayer contaminants within van der waals heterostructures. *ACS Applied Materials and Interfaces* **11**, 25578–25585 (2019). DOI: 10.1021/acsami.9b06594.

[63] Khestanova, E., Guinea, F., Fumagalli, L., Geim, A. K. & Grigorieva, I. V. Universal shape and pressure inside bubbles appearing in van der waals heterostructures. *Nature Communications* **7**, 12587 (2016). DOI: 10.1038/ncomms12587.

[64] Williams, D. B. & Carter, C. B. *Transmission Electron Microscopy* (Springer US, 2009).

[65] Brydson, R. *Aberration-Corrected Analytical Transmission Electron Microscopy* (Wiley, 2011).

[66] Broglie, L. D. Recherches sur la théorie des quanta. *Annales de Physique* **10**, 22–128 (1925). DOI: 10.1051/anphys/192510030022.

[67] Emmrich, D. *et al.* Nanopore fabrication and characterization by helium ion microscopy. *Applied Physics Letters* **108**, 163103 (2016). DOI: 10.1063/1.4947277.

[68] Zuo, J. M. *Advanced transmission electron microscopy : imaging and diffraction in nanoscience* (Springer, 2017).

[69] Sohlberg, K., Pennycook, T. J., Zhou, W. & Pennycook, S. J. Insights into the physical chemistry of materials from advances in haadf-stem. *Physical Chemistry Chemical Physics* **17**, 3982–4006 (2015). DOI: 10.1039/c4cp04232h.

[70] Susi, T., Meyer, J. C. & Kotakoski, J. Quantifying transmission electron microscopy irradiation effects using two-dimensional materials. *Nature Reviews Physics* **1**, 397–405 (2019). DOI: 10.1038/s42254-019-0058-y.

[71] Vierimaa, V., Krasheninnikov, A. V. & Komsa, H. P. Phosphorene under electron beam: From monolayer to one-dimensional chains. *Nanoscale* **8**, 7949–7957 (2016). DOI: 10.1039/c6nr00179c.

[72] Kretschmer, S., Lehnert, T., Kaiser, U. & Krasheninnikov, A. V. Formation of defects in two-dimensional mos2 in the transmission electron microscope at electron energies below the knock-on threshold: The role of electronic excitations. *Nano Letters* **20**, 2865–2870 (2020). DOI: 10.1021/acs.nanolett.0c00670.

[73] Speckmann, C. *et al.* Combined electronic excitation and knock-on damage in monolayer mos2. *Physical Review B* **107**, 094112 (2023). DOI: 10.1103/PhysRevB.107.094112.

[74] Hage, F. S., Radtke, G., Kepaptsoglou, D. M., Lazzeri, M. & Ramasse, Q. M. Single-atom vibrational spectroscopy in the scanning transmission electron microscope. *Science* **367**, 1124–1127 (2020). DOI: 10.1126/science.aba1136.

[75] Scherzer, O. Über einige fehler von elektronenlinsen. *Zeitschrift für Physik* **101**, 593–603 (1936). DOI: 10.1007/BF01349606.

[76] Krivanek, O. L., Lovejoy, T. C. & Dellby, N. Aberration-corrected stem for atomic-resolution imaging and analysis. *Journal of Microscopy* **259**, 165–172 (2015). DOI: 10.1111/jmi.12254.

[77] Scheinecker, D. Tem saed analysis of corrugations in low-dimensional materials (2019).

[78] www.eels.info/atlas accessed on 02.05.2023.

[79] Fultz, B. & Howe, J. M. *Transmission Electron Microscopy and Diffractometry of Materials* (Springer, 2008).

[80] Pizzocchero, F. *et al.* The hot pick-up technique for batch assembly of van der waals heterostructures. *Nature Communications* **7**, 11894 (2016). DOI: 10.1038/ncomms11894.

[81] Kinoshita, K. *et al.* Dry release transfer of graphene and few-layer h-bn by utilizing thermoplasticity of polypropylene carbonate. *npj 2D Materials and Applications* **3**, 22 (2019). DOI: 10.1038/s41699-019-0104-8.

[82] Bøggild, P. Research on scalable graphene faces a reproducibility gap. *Nature Communications* **14**, 1126 (2023). DOI: 10.1038/s41467-023-36891-5.

[83] Castellanos-Gomez, A. *et al.* Deterministic transfer of two-dimensional materials by all-dry viscoelastic stamping. *2D Materials* **1**, 011002 (2014). DOI: 10.1088/2053-1583/1/1/011002.

[84] Meitl, M. A. *et al.* Transfer printing by kinetic control of adhesion to an elastomeric stamp. *Nature Materials* **5**, 33–38 (2006). DOI: 10.1038/nmat1532.

[85] Hong, J. *et al.* Origin of new broad raman d and g peaks in annealed graphene. *Scientific Reports* **3**, 2700 (2013). DOI: 10.1038/srep02700.

[86] Trentino, A. *et al.* Atomic-level structural engineering of graphene on a mesoscopic scale. *Nano Letters* **21**, 5179–5185 (2021). DOI: 10.1021/acs.nanolett.1c01214.

[87] www.pubchem.ncbi.nlm.nih.gov/compound/9989226 accessed on 02.05.2023.

[88] www.lithoz.com accessed on 02.05.2023.

[89] Clark, N. *et al.* Scalable patterning of encapsulated black phosphorus. *Nano Letters* **18**, 5373–5381 (2018). DOI: 10.1021/acs.nanolett.8b00946.

[90] Qin, G. *et al.* Anisotropic intrinsic lattice thermal conductivity of phosphorene from first principles. *Physical Chemistry Chemical Physics* **17**, 4854–4858 (2015). DOI: 10.1039/c4cp04858j.

[91] Das, P. M. *et al.* Controlled sculpture of black phosphorus nanoribbons. *ACS Nano* **10**, 5687–5695 (2016). DOI: 10.1021/acsnano.6b02435.

[92] Leuthner, G. T. *et al.* Scanning transmission electron microscopy under controlled low-pressure atmospheres. *Ultramicroscopy* **203**, 76–81 (2019). DOI: 10.1016/j.ultramic.2019.02.002.

[93] Hettler, S. *et al.* Carbon contamination in scanning transmission electron microscopy and its impact on phase-plate applications. *Micron* **96**, 38–47 (2017). DOI: 10.1016/j.micron.2017.02.002.

[94] Mitchell, D. R. Contamination mitigation strategies for scanning transmission electron microscopy. *Micron* **73**, 36–46 (2015). DOI: 10.1016/j.micron.2015.03.013.

[95] Meyer, J. C. *et al.* Accurate measurement of electron beam induced displacement cross sections for single-layer graphene. *Physical Review Letters* **108**, 196102 (2012). DOI: 10.1103/PhysRevLett.108.196102.

[96] Susi, T. *et al.* Isotope analysis in the transmission electron microscope. *Nature Communications* **7**, 13040 (2016). DOI: 10.1038/ncomms13040.

[97] Åhlgren, E. H. *et al.* Atomic-scale oxygen-mediated etching of 2d mos2 and mote2. *Advanced Materials Interfaces* **9**, 2200987 (2022). DOI: 10.1002/admi.202200987.

[98] Wang, W. Polymer-free assembly of ultraclean van der waals heterostructures. *Nature Reviews Physics* **4**, 504–504 (2022). DOI: 10.1038/s42254-022-00458-y.

Construction plan of the aloxide oven (all lengths in mm)

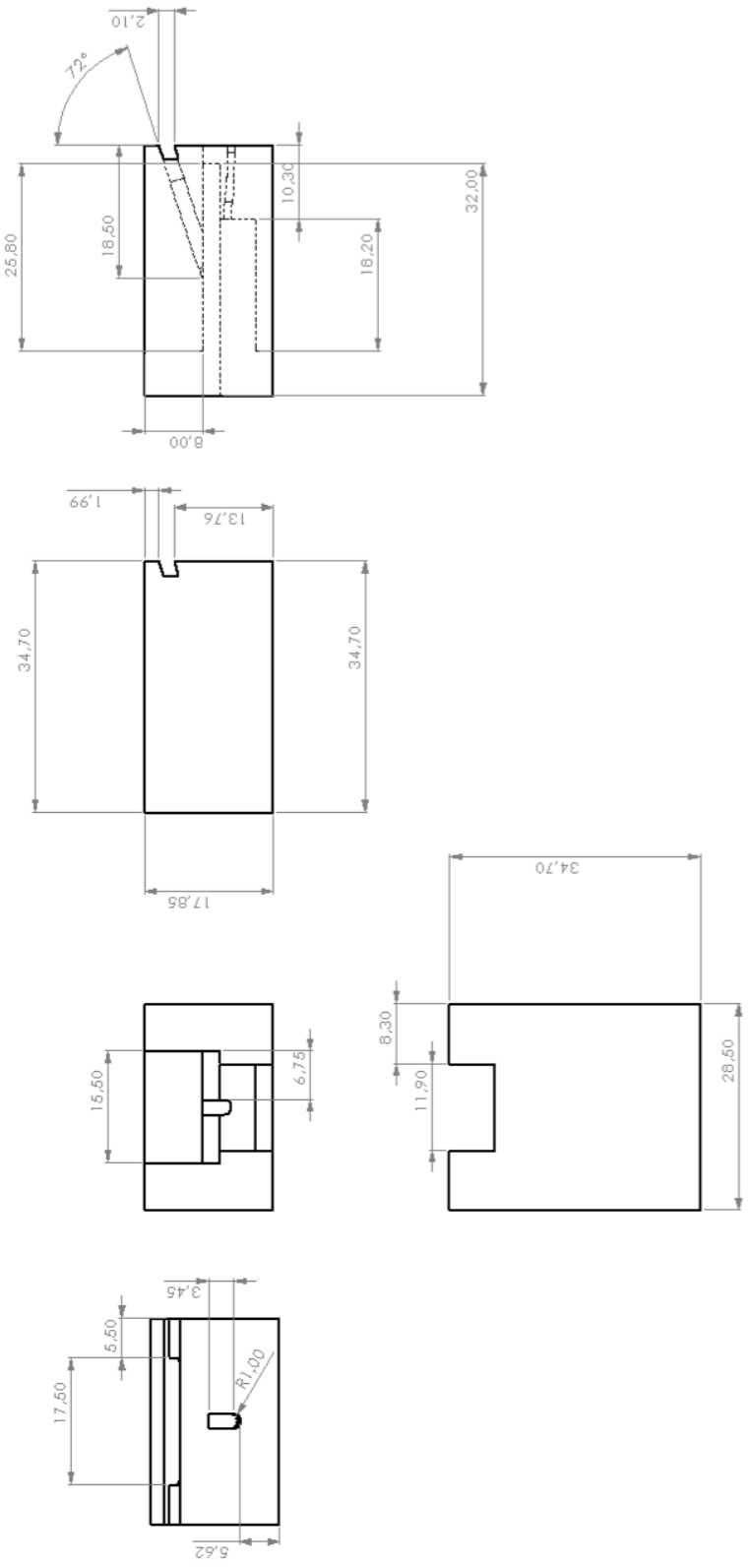

Construction plan of the frame (all lengths in mm)

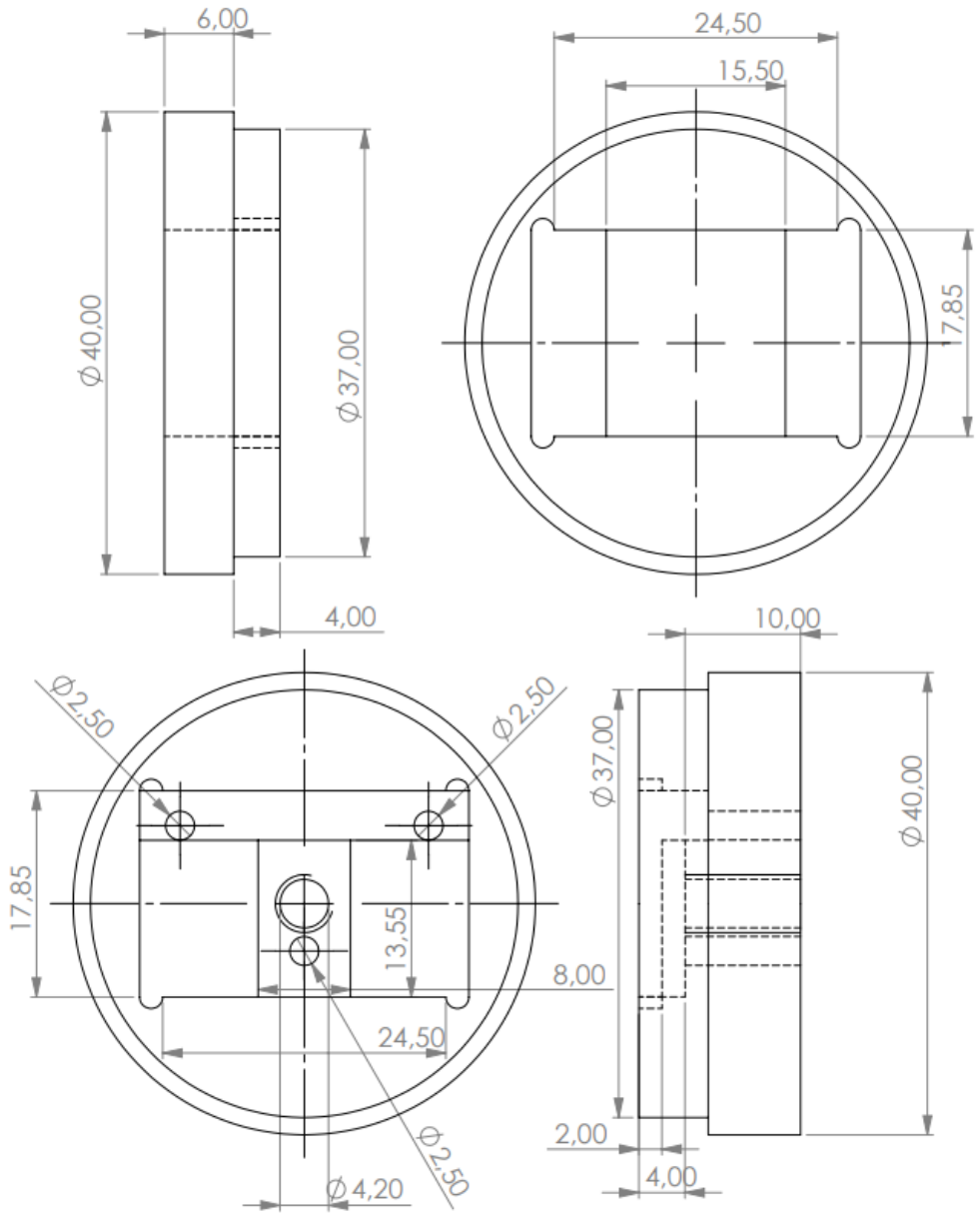

Raw data and baselines of the EELS measurements

Contamination cluster Oxygen

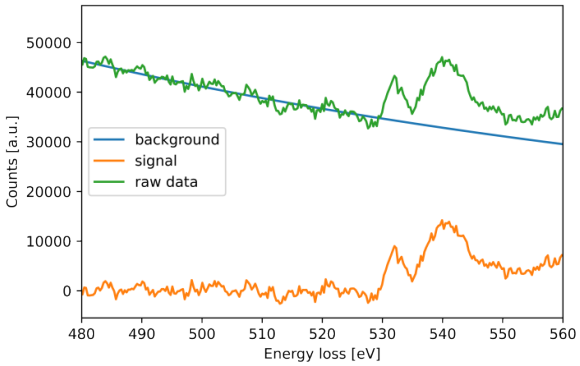

Dirt Pocket Oxygen

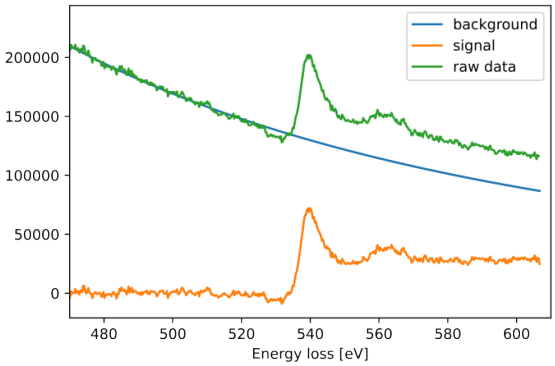

Sample surface Phosphorus

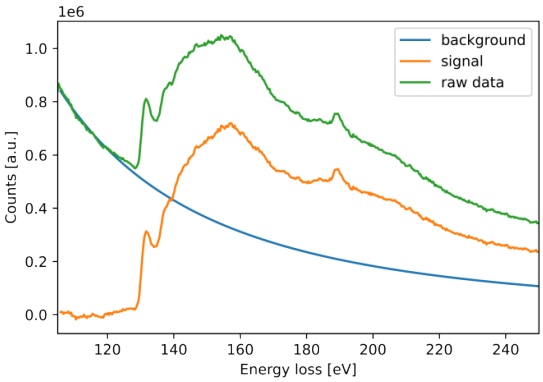

Sample surface Oxygen

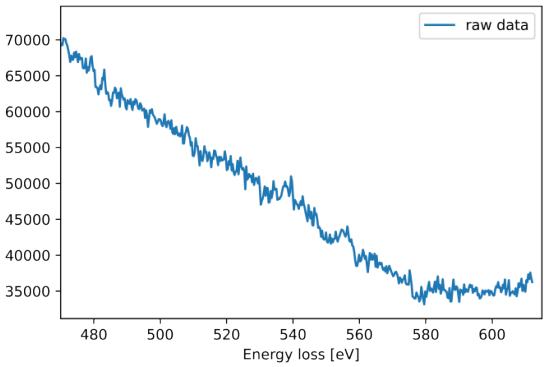

Fresh sample Oxygen

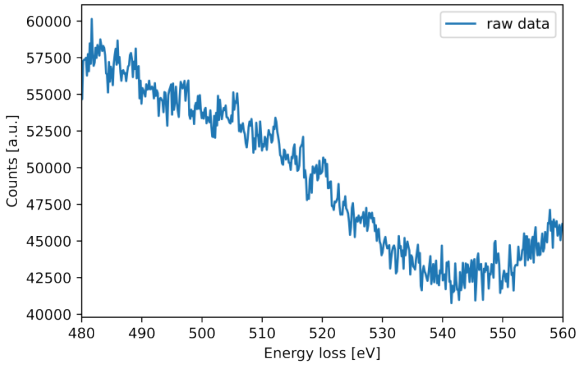

Fresh sample Phosphorus